
Energy-Guided Flow Matching Enables Few-Step Conformer Generation and Ground-State Identification

Guikun Xu¹, Xiaohan Yi³, Peilin Zhao^{1,✉}, Yatao Bian^{2,✉}

¹School of Artificial Intelligence, Shanghai Jiao Tong University, Shanghai, China

²Department of Computer Science, National University of Singapore, Singapore

³Shenzhen International Graduate School, Tsinghua University, Shenzhen, China

✉ : richxu945@sjtu.edu.cn

✉ : peilinzhaosjtu.edu.cn; ybian@nus.edu.sg

GitHub : <https://github.com/Rich-XGK/EnFlow.git>

Abstract

Generating low-energy conformer ensembles and identifying ground-state conformations from molecular graphs remain computationally demanding with physics-based pipelines. Current learning-based approaches often suffer from a fragmented paradigm: generative models capture diversity but lack reliable energy calibration, whereas deterministic predictors target a single structure and fail to represent ensemble variability. Here we present **EnFlow**, a unified framework that couples flow matching (FM) with an explicitly learned energy model through an energy-guided sampling scheme defined along a non-Gaussian FM path. By incorporating energy-gradient guidance during sampling, our method steers trajectories toward lower-energy regions, substantially improving conformational fidelity, particularly in the *few-step* regime. The learned energy function further enables efficient energy-based ranking of generated ensembles for accurate ground-state identification. Extensive experiments on GEOM-QM9 and GEOM-Drugs demonstrate that **EnFlow** simultaneously improves generation metrics with 1–2 ODE-steps and reduces ground-state prediction errors compared with state-of-the-art methods.

1 Introduction

Given a molecular topological graph specifying atom and bond types, the three-dimensional coordinates of its atoms define the set of possible molecular conformations. These conformations are essential for interpreting chemical properties and biological functions [1, 2]. Identifying energetically favorable conformations is a central problem in computational chemistry and drug discovery [3]. Conventional approaches, including molecular dynamics simulations [4, 5, 6] and density functional theory [7] optimizations, are computationally intensive and time-consuming, which limits their applicability to large-scale studies. Among low-energy structures, the ground-state conformation is the global minimum of the potential energy surface [8] and thus the most thermodynamically stable. It plays a key role in determining binding affinities, reaction mechanisms, and spectroscopic properties. Therefore, its accurate identification is essential for reliable prediction and rational molecular design.

Recent years have witnessed concerted efforts to harness advances in machine learning [9, 10, 11], particularly deep generative modeling [12, 13, 14, 15, 16, 17, 18], to address conformer generation with substantially improved computational efficiency [14, 15, 16, 17, 18, 19]. Although early learning-based approaches often underperformed [20, 21, 22, 23, 24, 25],

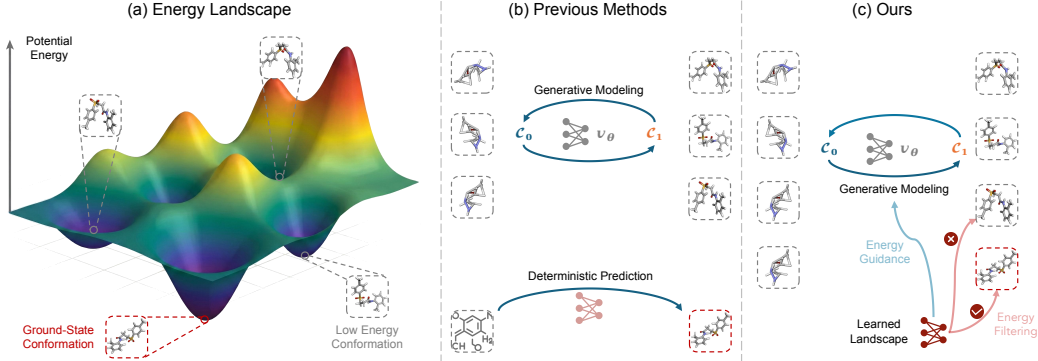


Figure 1: (a) Potential energy landscape of molecular conformations: low-energy conformers populate local minima, and the ground-state conformation corresponds to the global minimum. (b) Existing generative methods can sample diverse low-energy conformers but struggle to reliably identify the ground state, whereas deterministic methods predict a single structure near the ground state and fail to capture the ensemble variability. (c) Our **EnFlow** framework unifies both capabilities: it efficiently generates low-energy conformational ensembles and accurately identifies the ground-state conformation by leveraging a learned, explicit energy function that simultaneously guides the generative process.

GeoDiff [26] introduced a principled equivariant diffusion [14, 16, 27, 28] formulation for molecular structures. Building on this foundation, flow matching [17] has emerged as an alternative to diffusion models [16] and yields superior sample efficiency and faster generation [17, 18]. Subsequent studies further refine flow-matching pipelines to attain a more favorable balance between conformational fidelity and computational cost [29, 30].

Despite substantial progress in identifying low-energy conformations for a given molecular graph, pinpointing the global minimum, the ground-state conformation, remains challenging. To address this challenge, recent studies employ deterministic prediction methods that model the ground state directly, which reduces reliance on stochastic sampling and subsequent ranking. In these approaches [31, 32, 33, 34, 35], deterministic neural networks, particularly Graph Transformers [36] with task-specific modifications, are trained to regress the ground-state conformation from datasets that provide a single ground-state label for each molecule.

As shown in Fig. 1(b), a practical method that jointly models the low-energy conformational ensemble and the specific ground state within a single unified framework remains lacking. Generative approaches [26, 29] can sample diverse structures but do not provide an explicit, calibrated view of the energy landscape, making ground-state identification unreliable. Prediction approaches [32, 35], by contrast, predict a single structure intended to approximate the ground state and therefore fail to capture ensemble variability or quantify uncertainty.

To address the above challenges, we propose **EnFlow**, as illustrated in Fig. 1(c), a unified framework for generating low-energy molecular conformational ensembles, together with a demonstrably fast learning-based certification of the ground-state conformation. Fig. 2 provides an overview of EnFlow:

- (1) An energy-guided FM framework is proposed to enable principled guidance along non-Gaussian FM paths, providing a unified solution to the conformation problems described above. Unlike conventional guidance techniques developed for Gaussian-path FM and Diffusion models [37, 38, 39], such approaches do not directly extend to non-Gaussian settings. In conformation modeling, the prior distribution often deviates substantially from a Gaussian prior (e.g., the *Harmonic Prior* [40]), reflecting strong domain-specific structural inductive biases that are essential for capturing molecular structure and consequently inducing flow dynamics that differ fundamentally from the Gaussian-path regime.
- (2) An energy-based guidance mechanism is formulated to incorporate energy information directly into the flow dynamics. Samples are thereby steered toward lower-energy regions, leading to substantially improved sample fidelity, particularly under few-step ODE sampling.
- (3) A central component of the framework is an explicit energy function that models the conformational energy landscape. This function is parameterized using an energy-based

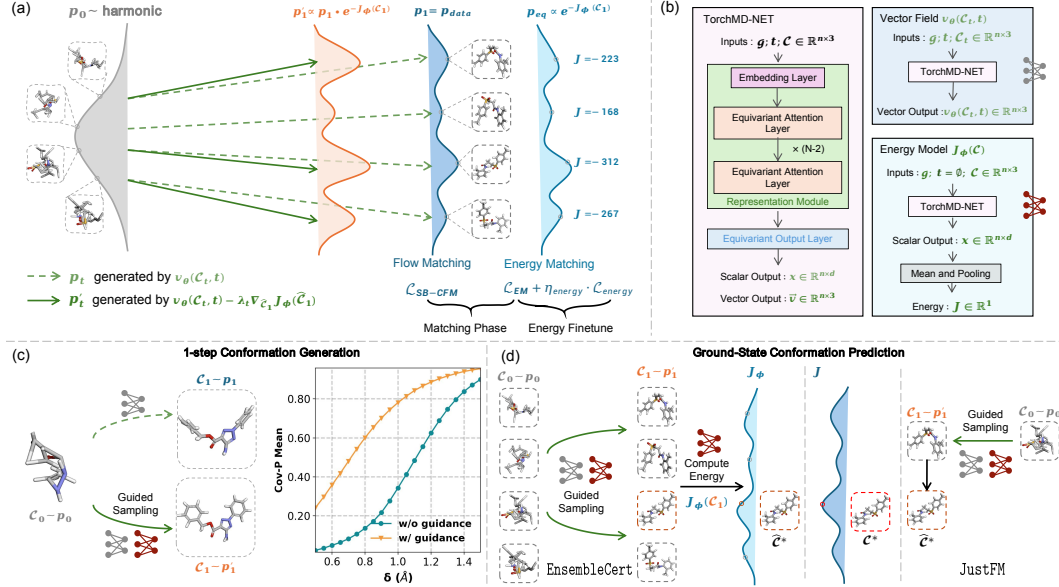


Figure 2: **EnFlow** illustrations. (a) The *energy-guided flow matching* framework, in which an EBM trained via the Energy Matching technique provides guidance during the flow matching process. (b) Architectural overview of the vector field and the energy model. For comparision fairness, we used the same backbone architecture as that of ET-Flow [29] (c) Illustration of improved one-step ODE sampling achieved through energy-guided sampling. (d) Using the well-trained energy function to certify the ground-state conformation.

model (EBM)[41], trained via the recently proposed *Energy Matching* objective [42]. Beyond capturing the global energy structure, the EBM is further fine-tuned to match empirical per-molecule energy distributions, enabling the resolution of subtle energy variations across different conformations of the same molecule. (4) Beyond improved ensemble generation, coupling a strong generator with a well-aligned EBM endows EnFlow with an explicit and calibrated energy function. This enables efficient ground-state identification either by ranking generated conformations according to predicted energies or by direct one-shot generation that produces a single conformation per molecule using the proposed energy-guided sampling procedure. In this work, the proposed framework is instantiated using ET-Flow [29] with a *Harmonic Prior* [40] as the generative backbone, transporting harmonic samples to physically plausible molecular conformations.

Supported by empirical experiments on GEOM-QM9 and GEOM-Drugs, EnFlow achieves SOTA performance in both small-scale and large-scale settings for 1–2 ODE-steps conformational ensemble generation and for ground-state conformation prediction, significantly surpassing existing methods. By acting as a fast, differentiable surrogate for quantum mechanics, EnFlow paves the way for biologically aware and thermodynamically consistent molecular design.

2 Results

While prior methods typically address conformation ensemble generation or ground-state certification in isolation, our approach unifies these two tasks within a single framework. We report comprehensive experimental results on the GEOM-QM9 and GEOM-Drugs datasets [43], demonstrating that the proposed **EnFlow** can simultaneously achieve strong performance on both tasks, thereby highlighting the effectiveness and practicality of the proposed unified approach. As illustrated in Fig. 3, on GEOM-Drugs, EnFlow is the first method to achieve strong performance in ground-state conformation prediction while maintaining balanced ensemble generation capability with a relatively small number of neural parameters compared to most existing methods. Sec. 2.3 presents detailed results on conformation generation, showing that our method maintains competitive performance while

achieving substantial improvements under few-step ODE sampling. Sec. 2.4 demonstrates that the learned energy model can effectively identify the lowest-energy conformation from the generated ensemble as the predicted ground-state structure, leading to significant performance gains. Sec. 2.5 further provides a rigorous analysis revealing that the learned energy function actively guides conformations toward lower-energy regions, underscoring its dual role in our unified framework: enabling guided generation and serving as a surrogate chemical model for energy-based screening. Additional experiments and discussions are provided in Sec. D.2.

2.1 Notations and Problem Definition

Main Notations: A 3D molecule is formally defined as $\mathcal{M} := \{\mathcal{G}, \mathcal{C}\}$, where \mathcal{G} denotes the 2D graph representation of the molecule, and $\mathcal{C} \in \mathbb{R}^{n \times 3}$ represents the conformation of the molecule in 3D space, specifically encompassing the spatial coordinates of each atom.

Problem Definition: The task of *molecular conformation generation* aims to generate an ensemble of potential low-energy stable conformations, $\mathcal{C}^1, \mathcal{C}^2, \dots$, for a given molecular graph \mathcal{G} . The objective is to model the conditional distribution $p(\mathcal{C}|\mathcal{G})$. For simplicity, in the following sections, we use the notation $p(\mathcal{C})$ to represent $p(\mathcal{C}|\mathcal{G})$. The task of *molecular ground-state conformation prediction* focuses on predicting the most stable conformation \mathcal{C}^* for the given molecular graph \mathcal{G} .

2.2 Datasets, Metrics, and Baselines

Datasets: In accordance with established practice, we evaluate our method on the **GEOM** datasets [43] using the splitting protocol defined in Refs. [24, 44]. Each molecule is associated with multiple low-energy conformations, and each conformation is annotated with a Boltzmann energy and an associated Boltzmann weight. Following Ref. [35], we define the ground-state conformation for each molecule as the conformer with the highest Boltzmann weight, and we use this definition to assess ground-state identification. The test sets for both the GEOM-QM9 and GEOM-Drugs subsets consist of 1,000 molecules. More details of datasets can be found in Sec. A.2.

Metrics for Conformer Ensemble Generation: This task is evaluated using four well-established metrics based on the Root Mean Square Deviation (RMSD) calculation: Coverage (COV) and Average Minimum RMSD (AMR) for both *Recall* and *Precision* protocols, namely COV-R, AMR-R, COV-P, and AMR-P. Following previous studies [24, 26, 45], let \mathcal{R} represent the reference set of K conformers, $\mathcal{R} = \{\mathcal{C}^1, \mathcal{C}^2, \dots, \mathcal{C}^K\}$, and \mathcal{G} denotes a generated set of $2K$ conformers, $\mathcal{G} = \{\hat{\mathcal{C}}^1, \hat{\mathcal{C}}^2, \dots, \hat{\mathcal{C}}^{2K}\}$. The Recall metrics are defined as follows:

$$\text{RMSD}(\mathcal{C}, \hat{\mathcal{C}}) = \sqrt{\frac{1}{n} \sum_{i=1}^n \|\mathcal{C}_i - \hat{\mathcal{C}}_i\|^2}, \quad (1)$$

$$\text{COV}(\mathcal{R}, \mathcal{G}) = \frac{|\{\mathcal{C}^k \in \mathcal{R} \mid \min_{\hat{\mathcal{C}}^j \in \mathcal{G}} \text{RMSD}(\mathcal{C}^k, \hat{\mathcal{C}}^j) < \delta\}|}{|\mathcal{R}|}, \quad (2)$$

$$\text{AMR}(\mathcal{R}, \mathcal{G}) = \frac{1}{|\mathcal{R}|} \sum_{\mathcal{C}^k \in \mathcal{R}} \min_{\hat{\mathcal{C}}^j \in \mathcal{G}} \text{RMSD}(\mathcal{C}^k, \hat{\mathcal{C}}^j), \quad (3)$$

where δ represents a threshold value, typically set to 0.5 Å for GEOM-QM9 and 0.75 Å for GEOM-Drugs. The Coverage metric quantifies the proportion of reference conformers in

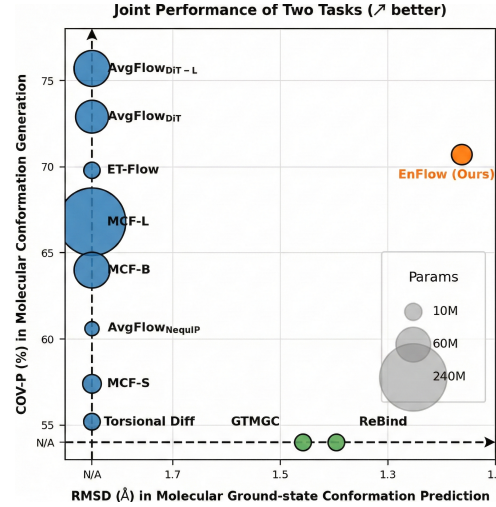


Figure 3: Joint performance on GEOM-Drugs across molecular conformation generation and ground-state conformation prediction tasks.

\mathbf{R} that have at least one generated conformer in \mathbf{G} within the threshold distance δ . The AMR metric computes the average minimum RMSD between each reference conformer in \mathbf{R} and its closest generated conformer in \mathbf{G} . The Recall metrics assess their diversity, while the Precision metrics, obtained by swapping the roles of \mathbf{R} and \mathbf{G} in the above equations, evaluate their quality.

Metrics for Ground-State Conformation Prediction: Given the ground-state conformation \mathcal{C}^* and its corresponding prediction $\hat{\mathcal{C}}^*$, following established works [32, 35], we adopt three standard metrics to evaluate the prediction performance: \mathcal{C} -RMSD, \mathbf{D} -MAE, and \mathbf{D} -RMSE. First, the RMSD between the predicted and ground-truth conformations is computed as in Eq. 1, yielding \mathcal{C} -RMSD. Then, let \mathbf{D}_{ij} and $\hat{\mathbf{D}}_{ij}$ denote the ground-truth and predicted pairwise distances, respectively. The Mean Absolute Error (MAE) and the Root Mean Squared Error (RMSE) between these distances are defined as follows:

$$\mathbf{D}\text{-MAE}(\mathcal{C}^*, \hat{\mathcal{C}}^*) = \frac{1}{n^2} \sum_{i=1}^n \sum_{j=1}^n \left| \mathbf{D}_{ij}^* - \hat{\mathbf{D}}_{ij}^* \right|, \quad (4)$$

$$\mathbf{D}\text{-RMSE}(\mathcal{C}^*, \hat{\mathcal{C}}^*) = \sqrt{\frac{1}{n^2} \sum_{i=1}^n \sum_{j=1}^n \left(\mathbf{D}_{ij}^* - \hat{\mathbf{D}}_{ij}^* \right)^2}. \quad (5)$$

Baselines: For *molecular conformer generation*, we first compare the best-performing configuration of our method against strong baselines, including GeoMol [24], GeoDiff [26], Torsional Diff [44], ET-Flow [45], MCF [46] and AvgFlow [30]. For 1 and 2 ODE sampling steps generation, we further compare with MCF [46], ET-Flow [29] and AvgFlow [30]. For *ground-state conformation prediction*, we benchmark against RDKit [47], GINE [48], GATv2 [49], GraphGPS [50], GTMGC [32], Torsional Diff [44] and ReBind [35], with all settings following Ref. [35]. For clarity, for ET-Flow [29] class of methods, ET-Flow denotes the model with a post hoc correction, while ET-Flow- $SO(3)$ indicates the $SO(3)$ -equivariant variant. Following this convention, we refer to our models as **EnFlow** and **EnFlow- $SO(3)$** . In AvgFlow [30], a few ODE sampling settings are benchmarked, and techniques such as Reflow and Distillation [18] are employed to achieve improved performance. Accordingly, the subscripts $\mathbb{X}_{\text{Reflow}}$ and $\mathbb{X}_{\text{Distill}}$ denote the application of these techniques to the method \mathbb{X} .

2.3 EnFlow Enhances Fidelity in Conformer Generation with Few ODE Steps

For the task of *generating low energy conformations ensemble*, we propose an *energy guided flow matching* scheme that transports the *Harmonic Prior* $p_0(\mathcal{C}_0)$ to the guided target distribution $p'_1(\mathcal{C}) \propto p_1(\mathcal{C}_1) e^{-J_\phi(\mathcal{C}_1)}$, rather than to the original data distribution $p_1(\mathcal{C}_1)$. With this design, from the perspective of ODE trajectories evolving from p_0 to p'_1 , the guided vector field $v'_t(\mathcal{C}_t)$ is discouraged from moving toward high-energy regions.

Results on GEOM-QM9: The performance of **EnFlow** on the GEOM-QM9 test set for *conformation generation* is reported in Tab. 1. The table presents the Coverage and AMR metrics defined in Eq. 2 and Eq. 3, respectively, with the RMSD threshold δ set to 0.5 Å. As shown, EnFlow- $SO(3)$ requires only 5 *ODE sampling steps* to achieve performance comparable to the previous baselines. With 50 *ODE sampling steps*, EnFlow- $SO(3)$ attains results similar to the best ET-Flow on Recall-oriented metrics, while outperforming ET-Flow on precision-oriented metrics; for example, it improves the mean COV-P by 1.43% (or by 0.71% compared with the reproduced ET-Flow- $SO(3)$ _{reproduced}). Notably, with only 2 *ODE sampling steps*, EnFlow- $SO(3)$ maintains comparable performance on Recall-oriented COV-R and AMR-R metrics, while achieving substantial improvements on Precision-oriented COV-P and AMR-P metrics, e.g., increasing the mean COV-P by 2.10% and reducing the mean AMR-P by 0.037 Å (24.34%) compared with ET-Flow- $SO(3)$. Furthermore, in the extreme case of 1 *ODE sampling step*, EnFlow is significantly superior to all existing methods, especially with unguided ET-Flow. Compared with the previous SOTA AvgFlow_{NequIP-D}, on Recall-oriented metrics, although EnFlow- $SO(3)$ shows an approximately 5% gap on COV-R,

Table 1: Molecule conformer generation results on GEOM-QM9 ($\delta = 0.5\text{\AA}$).

Methods	ODE steps	COV-R \uparrow		AMR-R \downarrow		COV-P \uparrow		AMR-P \downarrow	
		mean	median	mean	median	mean	median	mean	median
CGCF	1000	69.47	96.15	0.425	0.374	38.20	33.33	0.711	0.695
GeoDiff	1000	76.50	100.00	0.297	0.229	50.00	33.50	1.524	0.510
GeoMol	-	91.50	100.00	0.225	0.193	87.60	100.00	0.270	0.241
Torsional Diff.	20	92.80	100.00	0.178	0.147	92.70	100.00	0.221	0.195
MCF	1000	95.0	100.00	0.103	0.044	93.70	100.00	0.119	0.055
ET-Flow	50	96.47	100.00	0.073	0.047	94.05	100.00	0.098	0.039
ET-Flow-SO(3)	50	95.98	100.00	<u>0.076</u>	<u>0.030</u>	92.10	100.00	0.110	0.047
ET-Flow _{reproduced}	50	95.81	100.00	0.076	0.030	92.30	100.00	0.105	0.035
ET-Flow-SO(3) _{reproduced}	50	95.69	100.00	0.079	0.028	94.77	100.00	0.088	0.033
AvgFlow _{NequIP}	50	<u>96.40</u>	100.00	0.089	0.042	92.80	100.00	0.132	0.084
EnFlow	5	95.83	100.00	0.082	0.032	92.67	100.00	0.108	0.044
EnFlow	50	95.74	100.00	0.078	<u>0.030</u>	92.59	100.00	0.100	<u>0.036</u>
EnFlow-SO(3)	5	96.11	100.00	0.078	0.033	<u>95.11</u>	100.00	<u>0.090</u>	0.041
EnFlow-SO(3)	50	96.26	100.00	<u>0.076</u>	0.028	95.48	100.00	0.083	0.034
<i>2-step Generation</i>									
ET-Flow _{reproduced}	2	<u>96.27</u>	100.00	0.119	0.071	90.41	100.00	0.182	0.140
ET-Flow-SO(3) _{reproduced}	2	96.70	100.00	<u>0.112</u>	0.067	<u>93.54</u>	100.00	0.152	0.110
AvgFlow _{NequIP-R}	2	95.90	100.00	0.151	0.104	87.70	100.00	0.236	0.207
EnFlow	2	94.81	100.00	<u>0.112</u>	0.055	92.58	100.00	<u>0.138</u>	<u>0.075</u>
EnFlow-SO(3)	2	95.49	100.00	0.108	<u>0.058</u>	95.64	100.00	<u>0.115</u>	0.066
<i>1-step Generation</i>									
ET-Flow _{reproduced}	1	50.47	50.00	0.483	0.505	36.38	25.00	0.550	0.580
ET-Flow-SO(3) _{reproduced}	1	76.12	100.00	0.330	0.323	67.93	87.50	0.382	0.387
AvgFlow _{NequIP-D}	1	95.1	100.00	0.220	0.195	84.80	100.00	0.304	0.283
EnFlow	1	89.43	100.00	<u>0.215</u>	<u>0.178</u>	<u>88.09</u>	100.00	<u>0.256</u>	<u>0.227</u>
EnFlow-SO(3)	1	<u>90.45</u>	100.00	<u>0.195</u>	0.150	91.23	100.00	0.213	0.177
EnFlow-SO(3)_{Reflow}	1	96.70	100.00	<u>0.122</u>	<u>0.087</u>	<u>93.48</u>	100.00	<u>0.170</u>	<u>0.132</u>

Table notes. The results of the majority of baseline methods are reported in the corresponding literature. The method ET-Flow_{reproduced} and ET-Flow-SO(3)_{reproduced} denotes the results reproduced by us using the official ET-Flow [29] implementation. A detailed discussion of the reproduction issues is provided in Sec. D.1.3. For *2-step Generation* and *multi-step Generation*, the best results are highlighted in **bold**, and the second-best results are underlined. For *1-step Generation*, **EnFlow-SO(3)_{Reflow}** indicates performance obtained after an optional Reflow [18] technique on EnFlow; among the methods without Reflow, the best and second-best results are highlighted in **bold** and underlined, respectively.

it significantly reduces the mean AMR-R by 0.025 Å (11.36%) and the median AMR-R by 0.045 Å (23.08%); on Precision-oriented metrics, EnFlow-SO(3) improves the mean COV-P by 6.43% and reduces the mean AMR-P by 0.091 Å (29.93%) and the median AMR-P by 0.070 Å (24.73%). These results demonstrate the effectiveness of our energy-guided flow matching scheme in enhancing the fidelity of few ODE steps sampling for molecular conformer generation. Otherwise, after applying the Reflow technique [18] to EnFlow-SO(3) with 1 ODE step, the performance is further boosted, achieving the new SOTA results across all metrics, e.g., the mean COV-P is increased to 93.48%, and the mean AMR-P is reduced to 0.170 Å. Beyond evaluating these metrics at a fixed RMSD threshold, examining the curves of the coverage metrics COV-R and COV-P over varying RMSD thresholds provides a more comprehensive assessment. As reported in Fig. 8, we conduct ablation studies on whether to use our energy guidance (i.e., EnFlow-SO(3): **w/ guidance**) or not (i.e., ET-Flow-SO(3): **w/o guidance**) under 1, 2, and 5 ODE sampling steps. The results consistently show that, with our energy guidance, the coverage metrics are significantly improved at smaller RMSD thresholds, especially in the extremely low-step regime (i.e., 1 and 2 steps).

Results on GEOM-Drugs: The performance of **EnFlow** on the GEOM-Drugs is summarized in Tab. 2, where all metrics are evaluated under the RMSD threshold $\delta = 0.75\text{\AA}$. The table reports the Coverage and AMR metrics for both Recall- and Precision-oriented evaluations. As shown, with *50 ODE sampling steps*, EnFlow achieves competitive performance relative to existing diffusion- and flow-based approaches. In particular, its mean COV-R reaches 78.8% and the mean AMR-R is reduced to 0.475 Å, surpassing the reproduced ET-Flow_{reproduced}. On Precision-oriented metrics, EnFlow also maintains strong results, improving upon ET-Flow_{reproduced} on both COV-P and AMR-P, e.g., reducing the mean AMR-P from 0.604 Å to 0.590 Å. With only *5 ODE sampling steps*, EnFlow still achieves a

Table 2: Molecule conformer generation results on GEOM-Drugs ($\delta = 0.75\text{\AA}$).

Methods	ODE steps	COV-R \uparrow		AMR-R \downarrow		COV-P \uparrow		AMR-P \downarrow	
		mean	median	mean	median	mean	median	mean	median
GeoDiff	1000	42.10	37.80	0.835	0.809	24.90	14.50	1.136	1.090
GeoMol	-	44.60	41.40	0.875	0.834	43.00	36.40	0.928	0.841
Torsional Diff.	20	72.70	80.00	0.582	0.565	55.20	56.90	0.778	0.729
MCF - S (13M)	1000	79.4	87.5	0.512	0.492	57.4	57.6	0.761	0.715
MCF - B (64M)	1000	<u>84.0</u>	<u>91.5</u>	0.427	0.402	64.0	66.2	0.667	0.605
MCF - L (242M)	1000	84.7	92.2	0.390	0.247	66.8	71.3	0.618	0.530
ET-Flow (8.3M)	50	79.53	84.57	0.452	0.419	74.38	81.04	0.541	0.470
ET-Flow _{reproduced} (8.3M)	50	79.54	85.00	0.470	0.444	69.79	75.53	0.604	0.538
ET-Flow - SS (8.3M)	50	79.62	84.63	0.439	0.406	<u>75.19</u>	<u>81.66</u>	<u>0.517</u>	0.442
ET-Flow - SO(3) (9.1M)	50	78.18	83.33	0.480	0.459	67.27	71.15	0.637	0.567
AvgFlow _{NequiIP} (4.7M)	102	76.8	83.6	0.523	0.511	60.6	63.5	0.706	0.670
AvgFlow _{DiT} (52M)	100	82.0	86.7	0.428	0.401	72.9	78.4	0.566	0.506
AvgFlow _{DiT-L} (64M)	100	82.0	87.3	<u>0.409</u>	<u>0.381</u>	75.7	81.9	0.516	<u>0.456</u>
EnFlow (16.6M)	5	77.2	82.3	0.499	0.479	70.0	76.5	0.607	0.541
EnFlow (16.6M)	50	78.8	84.6	0.475	0.455	70.7	76.9	0.590	0.521
2-step Generation									
MCF-B (64M)	2	46.7	42.4	0.790	0.791	21.5	13.2	1.155	0.715
MCF-L (242M)	2	54.2	54.4	0.752	0.746	25.7	18.8	1.119	1.115
ET-Flow (8.3M)	2	<u>73.2</u>	<u>76.6</u>	<u>0.577</u>	<u>0.563</u>	<u>63.8</u>	<u>67.9</u>	<u>0.681</u>	<u>0.643</u>
ET-Flow _{reproduced} (8.3M)	2	72.3	76.9	0.592	0.583	58.3	60.4	0.733	0.699
AvgFlow _{NequiIP-Reflow} (4.7M)	2	64.2	67.7	0.663	0.661	43.1	38.9	0.871	0.853
AvgFlow _{DiT-Reflow} (52M)	2	75.7	81.8	0.545	0.533	57.2	59.0	0.748	0.705
EnFlow (16.6M)	2	70.7	74.6	0.596	0.578	<u>69.1</u>	<u>75.7</u>	<u>0.623</u>	<u>0.575</u>
1-step Generation									
MCF-B (64M)	1	22.1	6.9	0.962	0.967	7.6	1.5	1.535	1.541
MCF-L (242M)	1	27.2	13.6	0.932	0.928	8.9	2.9	1.511	1.514
ET-Flow (8.3M)	1	27.6	8.8	0.996	1.006	25.7	5.8	0.939	0.929
ET-Flow _{reproduced} (8.3M)	1	14.0	0.00	1.116	1.142	10.7	0.00	1.122	1.125
AvgFlow _{NequiIP-(Reflow+Distill)} (4.7M)	1	<u>55.6</u>	<u>56.8</u>	<u>0.739</u>	<u>0.734</u>	36.4	30.5	0.912	0.888
AvgFlow _{DiT-(Reflow+Distill)} (52M)	1	76.8	82.8	0.548	0.541	61.0	64.0	0.720	0.675
EnFlow (16.6M)	1	53.1	50.00	0.802	0.773	<u>54.3</u>	<u>56.3</u>	<u>0.773</u>	<u>0.743</u>
EnFlow_{Reflow} (16.6M)	1	74.3	80.0	0.566	0.548	60.6	63.5	0.719	0.666

Table notes. The results of the majority of baseline methods are reported in the corresponding literature. The *1-step Generation* and *2-step Generation* results of ET-Flow are reported from Ref. [30]. The method ET-Flow_{reproduced} denotes the results reproduced by us using the official ET-Flow [29] implementation. A detailed discussion of the reproduction issues is provided in Sec. D.1.3. For *2-step Generation* and *multi-step Generation*, the best results are highlighted in **bold**, and the second-best results are underlined. For *1-step Generation*, **EnFlow-SO(3)Reflow** indicates performance obtained after an optional Reflow [18] technique on EnFlow; among the methods without Reflow, the best and second-best results are highlighted in **bold** and underlined, respectively.

favorable Recall–Precision trade-off: its mean COV-R reaches 77.2% with a mean AMR-R of 0.499 Å, while on the Precision side it attains a mean COV-P of 70.0% and a mean AMR-P of 0.607 Å, substantially outperforming classical baselines such as GeoDiff, GeoMol, and Torsional Diffusion.

In the few-step regime, EnFlow demonstrates notable advantages. With *2 ODE sampling steps*, EnFlow achieves a mean COV-P of 69.1% and a mean AMR-P of 0.623 Å, outperforming all competing methods on Precision-oriented metrics, including ET-Flow and AvgFlow variants, while maintaining a strong mean COV-R of 70.7%. In the *1-step generation* scenario, EnFlow exhibits clear improvements over previous approaches: compared with ET-Flow_{reproduced}, EnFlow boosts the mean COV-P from 14.0% to 54.3% and reduces the mean AMR-P from 1.122 Å to 0.773 Å. Further applying the Reflow technique to our model (**EnFlow_{Reflow}**) yields additional gains and brings its performance close to the strongest AvgFlow variants: **EnFlow_{Reflow}** attains a mean COV-R of 74.3% and a mean AMR-R of 0.566 Å, together with a mean COV-P of 60.6% and a mean AMR-P of 0.719 Å, which is comparable to AvgFlow_{DiT-(Reflow+Distill)} while *requiring no extra distillation stage and using substantially fewer parameters* (16.6M vs. 52M). Overall, on GEOM-Drugs, EnFlow delivers competitive or superior performance in both the standard and few-step generation settings, with gains particularly pronounced in Precision-oriented metrics and extremely low-step ODE sampling. As shown in Fig. 9, we conduct ablation studies comparing the unguided baseline (ET-Flow; **w/o guidance**) and our energy-guided model (**EnFlow; w/ guidance**) under 1, 2, 5, and 50 ODE sampling steps. Consistently across all settings, energy guidance yields clear improvements in both COV-R and COV-P, particularly at smaller RMSD thresholds. The gains are most pronounced in the extremely low-step regime (i.e.,

Table 3: Ground-State Conformation Prediction Results on GEOM-Drugs (Å).

Methods	mode	Steps	D -MAE ↓	D -RMSE ↓	C -RMSD ↓
RDKit-DG	-	1	1.181	2.132	2.097
RDKit-ETKDG	-	1	1.120	2.055	1.934
GINE	-	1	1.125	1.777	2.033
GATv2	-	1	1.042	1.662	1.901
GraphGPS (RW)	-	1	0.879	1.399	1.768
GraphGPS (LP)	-	1	0.815	1.300	1.698
GTMGC	-	1	0.823	1.319	1.458
Torsional Diffusion	-	20	0.959	1.648	1.751
ReBind	-	1	0.776	<u>1.283</u>	1.396
ET-Flow	-	5	0.844 ± 0.009	1.491 ± 0.020	1.633 ± 0.011
EnFlow	JustFM	5	0.793 ± 0.011	1.412 ± 0.024	1.550 ± 0.029
EnFlow	EnsembleCert; $M = 5$	5	0.745	1.361	1.422
EnFlow	EnsembleCert; $M = 50$	50	0.714	1.296	1.338
EnFlow	EnsembleCert; $M = 50$	5	<u>0.703</u>	1.331	<u>1.312</u>
EnFlow	EnsembleCert; $M = 50$	50	0.644	1.263	1.163
SOTA improvement ↑	-	-	17.01%	1.56%	16.69%

Table notes. Results of Torsional Diffusion are taken from Ref. [35]. Results of ET-Flow and EnFlow (JustFM) are reported as mean \pm standard deviation over 10 independent runs, where each run generates a single conformation per molecule. Notably, generative methods without an energy-based selection step do not guarantee the generation of ground-state conformations, which contributes to the performance gap compared to discriminative prediction methods. Nevertheless, we evaluate their single-conformation generation error against the ground-state conformation label as a representative baseline here. For **EnFlow**, two inference modes are considered:

1. **JustFM**: Generates one conformation per molecule using our energy-guided sampling scheme.

2. **EnsembleCert**: Generates M conformations per molecule and selects the one with the lowest energy.

When the mode is **JustFM**, the guidance strength is set to $\lambda_t = 0.5(1-t)^2$ to prioritize precision in generation. For **EnsembleCert**, we use a smaller guidance strength $\lambda_t = 0.2(1-t)^2$ to promote diversity in the generated conformer ensemble, facilitating more effective selection.

1- and 2-step sampling), where the guided model lifts the coverage curves relative to the unguided baseline. These results further validate the effectiveness of our guidance strategy in enhancing few-step conformer generation on more complex molecules in GEOM-Drugs.

2.4 EnFlow Delivers Robust Ground-state Conformation Selection

Ground-State Conformation Prediction on GEOM-Drugs: Tab. 3 reports the ground-state conformation prediction results on GEOM-Drugs. Among existing methods, ReBind provides the strongest baseline performance. We first compare single-conformation generation under identical sampling budgets. With 5 sampling steps and one conformation per molecule, ET-Flow achieves \mathbf{D} -MAE = 0.844 ± 0.009 Å, \mathbf{D} -RMSE = 1.491 ± 0.020 Å, and \mathcal{C} -RMSD = 1.633 ± 0.011 Å, whereas EnFlow (JustFM) consistently improves all three metrics to \mathbf{D} -MAE = 0.793 ± 0.011 Å, \mathbf{D} -RMSE = 1.412 ± 0.024 Å, and \mathcal{C} -RMSD = 1.550 ± 0.029 Å, highlighting the effectiveness of energy-guided sampling even without ensemble selection. The proposed **EnsembleCert** scheme further reduces the errors with small ensembles and few sampling steps, and exhibits consistent performance gains as the ensemble size increases. In particular, with $M = 50$ and 50 steps, EnFlow establishes new state-of-the-art performance across all three metrics (\mathbf{D} -MAE = 0.644 Å, \mathbf{D} -RMSE = 1.263 Å, \mathcal{C} -RMSD = 1.163 Å), corresponding to relative improvements of 17.01%, 1.56%, and 16.69% over the previous best, respectively. Fig. 10 further shows that increasing the ensemble size M consistently reduces \mathbf{D} -MAE, \mathbf{D} -RMSE, and \mathcal{C} -RMSD, with especially pronounced gains when increasing M from 1 to 20 under 1–5 ODE steps. Notably, even with very few sampling steps, a sufficiently large ensemble can approach the accuracy of much longer sampling, indicating that the learned energy function $J_\phi(\mathcal{C})$ is highly discriminative and enables effective screening and ranking of low-energy conformations for ground-state prediction on GEOM-Drugs.

2.5 A Well-Learned Energy Landscape Guides Conformations Toward Lower Energies

Our goal is to learn a well-shaped energy landscape that captures energy variations of molecular conformations and yields nearly straight gradient directions from prior noise (Harmonic Prior samples) toward low-energy data. To this end, we use the *Energy Matching*

loss [42] to regularize regions off the data manifold and an energy regression loss to refine the landscape near the manifold. In Fig. 11, we perform an ablation on three variants of EnFlow on GEOM-Drugs with 5 ODE sampling steps: (1) an unguided baseline (ET-Flow; **w/o guidance**); (2) a guided model where J_ϕ is trained only with \mathcal{L}_{em} (**EnFlow: guidance & \mathcal{L}_{em}**); and (3) a fully guided model trained with both losses (**EnFlow: guidance & \mathcal{L}_{em} & $\mathcal{L}_{\text{energy}}$**). We generate one conformation per molecule and compute its error against the ground-state conformation, repeating the experiment 10 times to obtain statistics. As shown in the main \mathcal{C} -RMSD metric, the full model (**guidance & \mathcal{L}_{em} & $\mathcal{L}_{\text{energy}}$**) achieves the lowest median error and a clearly reduced spread compared with both the unguided baseline and the *Energy-Matching-only* variant. A similar trend is observed for **D-MAE** and **D-RMSE**, where the full model shifts the error distributions toward smaller values. These results indicate that the combined training objective encourages J_ϕ to guide sampling toward lower-energy conformations, thereby reducing discrepancies from the ground-state structures. Moreover, Fig. 12 visualizes the learned energy landscape on six randomly selected molecules and ablates the effect of guidance during ensemble sampling (**w/ guidance** vs. **w/o guidance**). In Fig. 12(b), the true energy profile and the predictions of J_ϕ for the ground-truth conformations (both normalized to $[0, 1]$) show that the learned energy function closely tracks the true energy variations. Fig. 12(c) and Fig. 12(d) further compare the predicted energy distributions of conformations generated with 2 and 5 ODE sampling steps: in both cases, guidance shifts the ensembles toward lower energies and reduces their spread, with a more pronounced concentration in the 5-step setting. This confirms that J_ϕ effectively steers sampling toward low-energy conformations.

2.6 More Results and Analysis

Additional experimental results and analyzes are provided in Sec. D.2. In particular, we (i) discuss the choice of the guidance schedule λ_t in Sec. D.2.1, (ii) justify the necessity of *Energy Matching* training in Sec. D.2.2, and (iii) demonstrate the robustness of the *energy-guided vector field* in EnFlow for sampling compared to alternative vector fields in Sec. D.2.3.

3 Preliminaries

3.1 Conditional Flow Matching

Given a source distribution $p_0 : \mathbb{R}^d \rightarrow \mathbb{R}_{\geq 0}$ and a target distribution $p_1 : \mathbb{R}^d \rightarrow \mathbb{R}_{\geq 0}$, probability flow models [17, 51, 52] introduce a *time-dependent* vector field (VF) $v_t(x_t) : [0, 1] \times \mathbb{R}^d \rightarrow \mathbb{R}^d$, which governs the evolution of a marginal probability path $p_t(x_t) : [0, 1] \times \mathbb{R}^d \rightarrow \mathbb{R}_{\geq 0}$, facilitating the transition of x_t from p_0 to p_1 as t progresses from 0 to 1. Both p_t and v_t must satisfy the following *continuity equation*:

$$\frac{\partial p_t(x_t)}{\partial t} + \nabla \cdot (p_t(x_t)v_t(x_t)) = 0. \quad (6)$$

Flow Matching (FM) [17, 51] is designed to learn a VF $v_\theta(x_t, t)$, parameterized by a neural network, that approximates the true VF $v_t(x_t)$ by minimizing the following *flow matching loss*:

$$\mathcal{L}_{\text{FM}} = \mathbb{E}_{t \sim \mathcal{U}(0,1), x_t \sim p_t} \left[\|v_\theta(x_t, t) - v_t(x_t)\|^2 \right]. \quad (7)$$

However, the true VF $v_t(x_t)$ is computationally intractable. In contrast, it is computationally feasible to define a *conditional vector field* $v_t(x_t|z)$, which generates a corresponding *conditional probability path* $p_t(x_t|z)$, where z serves as a conditioning variable, typically represented by a pair of source and target points, x_0 and x_1 [52]. The *conditional flow matching loss* can thus be formulated as:

$$\mathcal{L}_{\text{CFM}} = \mathbb{E}_{t \sim \mathcal{U}(0,1), x_t \sim p_t(x_t|z), z \sim p(z)} \left[\|v_\theta(x_t, t) - v_t(x_t|z)\|^2 \right]. \quad (8)$$

As demonstrated in Ref. [17], the gradients of the two losses are equivalent, i.e., $\nabla_\theta \mathcal{L}_{\text{FM}} = \nabla_\theta \mathcal{L}_{\text{CFM}}$. Therefore, after training with \mathcal{L}_{CFM} , the learned VF $v_\theta(x_t, t)$ can be used to generate samples by solving the ODE $dx_t = v_\theta(x_t, t) \cdot dt$ with $x_0 \sim p_0(x_0)$.

3.2 Energy Guided Flow Matching

Energy-Guided General Flow Matching: Given an energy function $J(x) : \mathbb{R}^d \rightarrow \mathbb{R}$, the energy-guided general (arbitrary source distribution) flow matching seeks to generate samples x from the guided distribution $p'(x) \propto p(x)e^{-J(x)}$. This approach is equivalent to using a new VF v'_t to generate a new probability path $p'_t(x_t)$, replacing the original VF v_t that generates $p_t(x_t)$.

The new VF v'_t is defined as:

$$v'_t(x_t) = v_t(x_t) + g_t(x_t). \quad (9)$$

Theorem 3.1 (Theorem 3.1 of Ref. [53]). *Adding the guidance VF $g_t(x_t)$ to the original VF $v_t(x_t)$ will form VF $v'_t(x_t)$ that generates $p'_t(x_t) = \int p_t(x_t|z)p'(z)dz$, as long as $g_t(x_t)$ follows:*¹

$$g_t(x_t) = \int \left(\mathcal{P} \frac{e^{-J(x_1)}}{Z_t(x_t)} - 1 \right) v_{t|z}(x_t|z)p(z|x_t)dz, \quad (10)$$

$$\text{where } Z_t(x_t) = \int \mathcal{P} e^{-J(x_1)} p(z|x_t)dz. \quad (11)$$

Guidance for Gaussian Path FM (Diffusion) Assumption: The Independent Coupling Gaussian FM assumes that the source and target distributions are independent, i.e., $p(z) = p_0(x_0)p_1(x_1)$, with the source distribution being Gaussian, specifically $p_0(x_0) = \mathcal{N}(x_0; \mu, \Sigma)$. As is well-established in the literature, this formulation is equivalent to diffusion models that employ distinct noise strategies [54, 55]. At this stage, the energy guidance takes the form of $g_t(x_t) \propto \nabla_{x_t} Z_t(x_t)$, which is a key component in similar guidance techniques for diffusion models [37, 56, 57] within the Diffusion Posterior Sampling (DPS) framework [56]. Specifically, this is expressed as $\nabla_{x_t} \log p'_t(x_t) = \nabla_{x_t} \log p_t(x_t) - \nabla_{x_t} J(x_t)$, as detailed in Ref. [39], or equivalently by $v''_t(x_t) = (1-w)v_t(x_t) + w[a_t x_t + b_t \nabla_{x_t} J(x_t)]$, which generates $p''(x) \propto p(x)^{1-w} e^{-wJ(x)}$, as described in Ref. [54]. Here, w is a coefficient, and a_t, b_t are time schedules.

(Approximate) Guidance for None Gaussian Path FM Assumption: To simplify and make Eq. 10 more tractable, Ref. [53] propose approximating it by Taylor expansion, motivated by the intuition that the probability mass of $p(x_1|x_t)$ is centered around its mean. First, the normalizing constant $Z_t(x_t)$ in Eq. 11 can be approximated as follows:

$$Z_t(x_t) = \int \mathcal{P} e^{-J(x_1)} p(z|x_t)dz \approx e^{-J(\hat{x}_1)}, \quad \hat{x}_1 = \mathbb{E}_{x_0, x_1 \sim p(z|x_t)}[x_1]. \quad (12)$$

Next, the guidance VF $g_t(x_t)$ can be approximated as (proof in Sec. A.9 of Ref. [53]):

$$g_t(x_t) \approx -\mathbb{E}_{z \sim p(z|x_t)} \left[(x_1 - \hat{x}_1) v_{1|t}(x_t|z) \right] \nabla_{\hat{x}_1} J(\hat{x}_1), \quad \hat{x}_1 = \mathbb{E}_{x_0, x_1 \sim p(z|x_t)}[x_1]. \quad (13)$$

For the non-Gaussian Path FM (i.e., with a non-Gaussian p_0), assuming the conditional probability path follows the widely used affine path, i.e., $x_t = \alpha_t x_1 + \beta_t x_0 + \sigma_t \epsilon$, where $\epsilon \sim \mathcal{N}(0, I)$ and $\sigma_t, \dot{\sigma}_t$ are both small [17, 52]. According to Ref. [51], \hat{x}_1 can be expressed by the x_1 -parameterization with the vector field v_t [53] as:

$$\hat{x}_1 \approx -\frac{\dot{\beta}_t}{\dot{\alpha}_t \beta_t - \dot{\beta}_t \alpha_t} x_t + \frac{\beta_t}{\dot{\alpha}_t \beta_t - \dot{\beta}_t \alpha_t} v_t(x_t). \quad (14)$$

By combining this with $v_{1|t}(x_t|z) = \dot{\alpha}_t x_1 + \dot{\beta}_t x_0 + \dot{\sigma}_t \epsilon$, the approximate guidance $g_t(x_t)$ can be reformulated as a product of the covariance matrix $\Sigma_{1|t}$ of $p(x_1|x_t)$, and the gradient

¹ $Z = \int e^{-J(x)} p(x)dx$ is the normalization constant. $\mathcal{P} = \frac{\pi'(x_0|x_1)}{\pi(x_0|x_1)}$ is the reverse coupling ratio, where $\pi'(x_0|x_1)$ is the reverse data coupling for the new VF, i.e., the distribution of x_0 given x_1 sampled from the target distribution. $\mathcal{P} = 1$ when $\pi(x_0, x_1) = p(x_0)p(x_1)$, i.e., set $p(z) = p_0(x_0)p_1(x_1)$ to be the *independent coupling* [52, 53].

$\nabla_{\hat{x}_1} J(\hat{x}_1)$ (proof in Sec. A.11 of Ref. [53]):

$$g_t(x_t) \approx -\frac{\alpha_t \beta_t - \dot{\beta}_t \alpha_t}{\beta_t} \cdot \Sigma_{1|t} \cdot \nabla_{\hat{x}_1} J(\hat{x}_1). \quad (15)$$

As suggested in Ref. [53], $\Sigma_{1|t}$ can be approximated as a manually defined schedule. This approach mirrors the guidance techniques employed in traditional diffusion models [54, 55] for the non-Gaussian Path FM, resulting in the following expression:

$$g_t(x_t) \approx -\lambda_t \cdot \nabla_{\hat{x}_1} J(\hat{x}_1). \quad (16)$$

Thus, the energy-guided VF $v'_t(x_t)$ for the non-Gaussian Path FM can be approximated as:

$$v'_t(x_t) \approx v_t(x_t) - \lambda_t \cdot \nabla_{\hat{x}_1} J(\hat{x}_1), \quad (17)$$

where λ_t is suggested to decay to zero as $t \rightarrow 1$, and \hat{x}_1 is given by the expression in Eq. 14.

4 Methodology

In this section, we present the methodology for our proposed approach, **EnFlow**, which predominantly utilizes the recently developed *Energy Matching* techniques [42] to jointly train an energy model $J_\phi(\mathcal{C})$ alongside the FM training process.² During the sampling process, the well-trained energy model $J_\phi(\mathcal{C})$ is employed to guide the reverse generation procedure.

4.1 Standard SB-CFM for Conformation Generation (ET-Flow)

We reinterpret ET-Flow [29] as the unguided FM framework for conformation generation, employing a standard *Schrödinger Bridge Conditional Flow Matching* (SB-CFM) path [52] to generate conformations from a non-Gaussian prior, specifically the *Harmonic Prior* [40, 58]. This methodology facilitates the generation of conformations in a straightforward yet high-performing manner.

Harmonic Prior: The *Harmonic Prior* [40, 58] enforces spatial proximity between atom positions that are connected by a bond. It is constructed based on covalent bonds, resulting in a molecular graph \mathcal{G} with an adjacency matrix $A \in [0, 1]^{n \times n}$, from which the graph Laplacian $L = D - A$ is derived, where D is the degree matrix. The harmonic prior is then expressed as $p_0(\mathcal{C}_0) \propto \exp\left(-\frac{1}{2}\mathcal{C}_0^T L \mathcal{C}_0\right)$.

SB-CFM Path: The SB-CFM path, introduced by Ref. [52], is formally defined as $p(z) = \pi_{2\sigma^2}(\mathcal{C}_0, \mathcal{C}_1)$, where $\pi_{2\sigma^2}$ represents the entropy-regularized optimal transport (OT) problem³ with the cost $\|\mathcal{C}_0 - \mathcal{C}_1\|$ and entropy regularization parameter σ^2 [59]. The SB-CFM path is characterized as a Brownian bridge with scale σ , bridging the configurations \mathcal{C}_0 and \mathcal{C}_1 . The associated conditional flow matching CFM path and the generating VF are then expressed as follows:

$$p_t(\mathcal{C}_t | \mathcal{C}_0, \mathcal{C}_1) = \mathcal{N}(\mathcal{C}_t; (1-t)\mathcal{C}_0 + t\mathcal{C}_1, t(1-t)\sigma^2 I), \quad (18)$$

$$v_t(\mathcal{C}_t | \mathcal{C}_0, \mathcal{C}_1) = \frac{1-2t}{2t(1-t)} \{ \mathcal{C}_t - [(1-t)\mathcal{C}_0 + t\mathcal{C}_1] \} + (\mathcal{C}_1 - \mathcal{C}_0). \quad (19)$$

After training the parameterized VF $v_\theta(\mathcal{C}_t, t)$ using the CFM loss:

$$\mathcal{L}_{\text{SB-CFM}} = \mathbb{E}_{\mathcal{C}_t \sim p_t(\mathcal{C}_t | \mathcal{C}_0, \mathcal{C}_1), t \sim \mathcal{U}(0, 1)} \left[\|v_\theta(\mathcal{C}_t, t) - v_t(\mathcal{C}_t | \mathcal{C}_0, \mathcal{C}_1)\|^2 \right], \quad (20)$$

with the initial condition $\mathcal{C}_0 \sim p_0(\mathcal{C}_0)$, the VF $v_\theta(\mathcal{C}_t, t)$ can be employed to generate conformations by solving the ODE, $d\mathcal{C}_t = v_\theta(\mathcal{C}_t, t) \cdot dt$.

²In this section, we reuse $\mathcal{C} \in \mathbb{R}^{n \times 3}$ to denote the data space instead of $x \in \mathbb{R}^d$ for conformation space generation, where ϕ represents the trainable parameters.

³In this context, \mathcal{C}_0 and \mathcal{C}_1 are not independent pairs, but rather are sampled according to the optimal transport cost π [52]. However, Ref. [53] demonstrates that $\mathcal{P} \approx 1$ is also a reasonable assumption for dependent optimal transport couplings (proof in Sec. A.3 of Ref. [53]).

4.2 Energy Matching for Efficiently Training EBMs

Energy-Based Models (EBMs): Energy-Based Models (EBMs) are a class of probabilistic models that define a probability distribution over data by associating an energy value with each data point. The energy function $J(\mathcal{C})$ to assign lower energy to more probable configurations. This defines a Boltzmann distribution $p(\mathcal{C}) \propto e^{-J(\mathcal{C})}$.

Energy Matching Nutshell: By examining the first-order optimality conditions [60, 61] of the Jordan–Kinderlehrer–Otto (JKO) scheme [62], Ref. [42] propose a novel framework that integrates the training of EBMs with the optimal transport (OT) framework, referred to as *Energy Matching*. The central idea is to learn a *time-independent scalar potential* $J_\phi(\mathcal{C})$ that defines a Boltzmann distribution $p(\mathcal{C}) \propto e^{-J_\phi(\mathcal{C})}$, which matches the data distribution $p_{data}(\mathcal{C})$. To transport noisy data $\mathcal{C}_0 \sim p_0(\mathcal{C}_0)$ to the data distribution $p_{data}(\mathcal{C})$, Ref. [42] propose two distinct phases:

- *Away from manifold:* In this phase, \mathcal{C}_0 is transported deterministically towards the data distribution $p_{data}(\mathcal{C})$ in an OT-like manner, at a constant speed. Specifically, $-\nabla_{\mathcal{C}_t} J_\phi(\mathcal{C}'_t) \approx \mathcal{C}_{data} - \mathcal{C}_0$, where the interpolation $\mathcal{C}'_t = (1-t)\mathcal{C}_0 + t\mathcal{C}_{data}$ is used, and $\mathcal{C}_{data} \sim p_{data}(\mathcal{C})$.
- *Near manifold:* In this phase, the samples evolve towards the Boltzmann distribution $p(\mathcal{C}) \propto e^{-J_\phi(\mathcal{C})}$, closely approximating the data distribution.

4.3 Jointly Training EBMs with SB-CFM

Matching Phase: Building upon the success of *Energy Matching* [42], we propose a joint training framework that simultaneously optimizes an energy model $J_\phi(\mathcal{C})$ and the SB-CFM training process. In this initial phase, the primary focus is on the matching losses associated with both the SB-CFM and the energy model. At each time step t , we first sample conformations $\mathcal{C}_0 \sim p_0(\mathcal{C}_0)$ and $\mathcal{C}_1 \sim p_1(\mathcal{C}_1)$, and then perform the following interpolation:

$$\mathcal{C}'_t = (1-t)\mathcal{C}_0 + t\mathcal{C}_1, \quad (21)$$

$$\mathcal{C}_t = \mathcal{C}'_t + \sigma \sqrt{t(1-t)} \cdot \epsilon, \quad \epsilon \sim \mathcal{N}(0, I). \quad (22)$$

Subsequently, the corresponding VFs are computed as follows:

$$S_t(\mathcal{C}'_t | \mathcal{C}_0, \mathcal{C}_1) = \mathcal{C}_1 - \mathcal{C}_0, \quad (23)$$

$$v_t(\mathcal{C}_t | \mathcal{C}_0, \mathcal{C}_1) = \frac{1-2t}{2t(1-t)} \{ \mathcal{C}_t - \mathcal{C}'_t \} + S_t. \quad (24)$$

Thus, the SB-CFM loss, denoted as $\mathcal{L}_{\text{SB-CFM}}$, is defined in Eq. 20, for clarity:

$$\mathcal{L}_{\text{SB-CFM}} = \mathbb{E}_{\mathcal{C}_t \sim p_t(\mathcal{C}_t | \mathcal{C}_0, \mathcal{C}_1), t \sim \mathcal{U}(0,1)} \left[\| v_\theta(\mathcal{C}_t, t) - v_t(\mathcal{C}_t | \mathcal{C}_0, \mathcal{C}_1) \|^2 \right]. \quad (25)$$

The energy matching loss is then computed as follows:

$$\mathcal{L}_{\text{EM}} = \mathbb{E}_{\mathcal{C}_0 \sim p_0(\mathcal{C}_0), \mathcal{C}_1 \sim p_1(\mathcal{C}_1), t \sim \mathcal{U}(0,1)} \left[\| -\nabla_{\mathcal{C}_t} J_\phi(\mathcal{C}'_t) - S_t(\mathcal{C}'_t | \mathcal{C}_0, \mathcal{C}_1) \|^2 \right]. \quad (26)$$

Energy Fine-tuning Phase: In the second phase, we focus on fine-tuning the energy model $J_\phi(\mathcal{C})$ to further enhance its capacity to accurately characterize the energy landscape of molecular conformations. It is worth noting that the approach proposed in Ref. [42] employs the traditional contrastive divergence (CD) loss in EBMs [63] to implicitly optimize the energy model toward the data distribution. However, this procedure is computationally intensive and often inefficient due to its reliance on MCMC-based negative sampling. *In our case, millions of molecules correspond to millions of distinct energy landscapes*, which results in substantial instability when training with the CD loss. Benefiting from the high-quality data provided by the GEOM dataset [43], each molecular conformation is accompanied by a corresponding Boltzmann energy label, obtained through high-level CREST+GFN2-xTB calculations with DFT fine-tuning (detailed in Sec. A.2). Therefore, we propose to directly

optimize the energy model via supervised learning, using the mean absolute error (MAE) between the predicted energy values and the ground-truth energy labels (normalized on a per-molecule basis). This loss serves as an auxiliary fine-tuning objective with a controllable weighting factor η_{energy} , while retaining \mathcal{L}_{EM} during this phase:

$$\mathcal{L}_{energy} = \mathbb{E}_{\mathcal{C} \sim p_{data}(\mathcal{C})} [|J_\phi(\mathcal{C}) - E_{true}(\mathcal{C})|], \quad (27)$$

$$\mathcal{L}_{fine-tune} = \mathcal{L}_{EM} + \eta_{energy} \cdot \mathcal{L}_{energy}. \quad (28)$$

This approach not only improves training efficiency but also enhances the accuracy of the energy model in capturing the energy landscape of molecular conformations, thereby achieving better alignment with true energy distributions in real-world applications.

Model Architectures: For fairness, we utilize the same model architectures as those employed in ET-Flow [29], specifically, TorchMD-NET [64] for both the energy model J_ϕ and the VF v_θ . TorchMD-NET generates both scalar features $x_i \in \mathbb{R}^d$ and vector features $\vec{v}_i \in \mathbb{R}^3$ for each atom i , such that $x, \vec{v} = \text{TorchMD-NET}(\mathcal{G}, \mathcal{C})$, where $x \in \mathbb{R}^{n \times d}$ and $\vec{v} \in \mathbb{R}^{n \times 3}$. For the energy model, we perform mean pooling on x and apply a linear layer to obtain the energy value, defined as $J_\phi(\mathcal{C}) = \text{Mean-Pooling}(x, \text{dim} = 0) \cdot W$, where $W \in \mathbb{R}^{d \times 1}$, and $(x, _) = \text{TorchMD-NET}_\phi(\mathcal{G}, \mathcal{C})$. For the VF, we directly use the vector features \vec{v} as the output, i.e., $v_\theta = \vec{v}$, where $(_, \vec{v}) = \text{TorchMD-NET}_\theta(\mathcal{G}, \mathcal{C})$. For details please refer to Sec. A.1 of Ref. [29] and Sec. C.

4.4 Energy-Guided Sampling for Conformation Generation

At this point, we have a well-trained energy model $J_\phi(\mathcal{C})$ and a VF $v_\theta(\mathcal{C}_t, t)$ that generates the probability path $p_t(\mathcal{C}_t | \mathcal{C}_0, \mathcal{C}_1)$ and transports a non-standard Gaussian prior $p_0(\mathcal{C}_0)$, i.e., the Harmonic Prior, to the true conformation distribution $p_1(\mathcal{C}_1)$. During the sampling process, the energy model can guide the reverse generation procedure by using the guided VF $v'_t(\mathcal{C}_t)$, as defined in Eq. 9, to transport $\mathcal{C}_0 \sim p_0(\mathcal{C}_0)$ to $\mathcal{C}'_1 \propto p_1(\mathcal{C}_1) e^{-J_\phi(\mathcal{C}_1)}$.

Based on Sec. 3.2 and Eq. 17, the approximate guided VF $v'_t(\mathcal{C}_t)$ is given by:

$$v'_t(\mathcal{C}_t) \approx v_\theta(\mathcal{C}_t, t) - \lambda_t \cdot \nabla_{\hat{\mathcal{C}}_1} J_\phi(\hat{\mathcal{C}}_1), \quad \hat{\mathcal{C}}_1 \approx \mathcal{C}_t + (1-t)v_\theta(\mathcal{C}_t, t), \quad (29)$$

where λ_t is a decay factor that approaches zero as $t \rightarrow 1$, and $\hat{\mathcal{C}}_1$ is defined by the reparameterization in Eq. 14. The sampling process can be summarized as:

$$\mathcal{C}_{t+\Delta t} = \mathcal{C}_t + v'_t(\mathcal{C}_t) \cdot \Delta t, \quad (30)$$

where $\mathcal{C}_0 \sim p_0(\mathcal{C}_0)$. This process continues until $t = 1$, at which point the generated conformations \mathcal{C}'_1 are expected to closely approximate the true conformations sampled from $p_1(\mathcal{C}_1)$, with lower energy values according to the energy model $J_\phi(\mathcal{C})$, i.e., $\mathcal{C}'_1 \propto p_1(\mathcal{C}_1) e^{-J_\phi(\mathcal{C}_1)}$. The overall sampling process is summarized in Alg. 2. Furthermore, since the schedule of λ_t is considered as a hyperparameter that decays to zero as $t \rightarrow 1$, we defer a more detailed discussion of the schedule for λ_t to Sec. D.1.4.

For more effective one-step sampling, Reflow [18] is a post-training technique that improves the quality of single-step sample generation. Following AvgFlow [30], we also apply the Reflow process along the SB-CFM path to further enhance the performance of one-step sampling. The detailed procedure is deferred to Sec. D.1.1.

4.5 Ground-State Conformation Certification

To enhance the practical utility of the generated conformations, we introduce a ground-state conformation certification step that aims to identify conformations likely to correspond to the global minimum energy state. This capability is essential for downstream applications such as drug discovery and materials design. We consider two complementary strategies for ground-state certification. (1) **JustFM** mode: We directly generate a single conformation per molecule in a one-shot manner using the energy-guided sampling process described in Alg. 2,

where the learned energy function explicitly steers the sampling trajectory toward low-energy regions. (2) **EnsembleCert** mode: Alternatively, given a molecular graph, we generate a conformational ensemble using the same energy-guided sampling procedure, and then identify the ground-state candidate by ranking the generated conformations according to the learned energy model $J_\phi(\mathcal{C})$. The detailed procedures are summarized in Alg. 3.

5 Limitations and Conclusion

Limitations. Although our method exhibits strong performance on both *molecular conformation generation* and *ground-state conformation prediction* within a unified framework, several limitations remain. First, from the viewpoint of ODE simulation (step size Δt), EnFlow enables high-quality few-step sampling by steering *harmonic-prior* samples toward the energy-guided distribution $p_1(\mathcal{C}_1)e^{-J_\phi(\mathcal{C}_1)}$ rather than the original $p_1(\mathcal{C}_1)$. However, the resulting inference time is substantially longer than that of unguided FM frameworks (e.g., ETFlow [29]), primarily due to the overhead of computing energy-model gradients. Second, although our method significantly reduces ground-state conformation prediction error through the learned energy landscape, its inference latency remains higher because FM (or diffusion-based) methods intrinsically require iterative sampling rather than a single forward evaluation. Third, the use of a Non-Gaussian prior (*Harmonic-Prior*) renders classical guidance techniques for Gaussian-path FMs inapplicable. Our proposed energy-guided mechanism therefore relies on the approximate Non-Gaussian guidance strategy of Ref. [53], whose optimality and controllability remain limited. Finally, while our framework is the first to jointly address both tasks in a unified manner, there is still considerable room for further improving task-specific performance. Future work will address these limitations to enhance the robustness, efficiency, and overall effectiveness of the proposed approach.

Conclusion. In this work, we challenge the prevailing paradigm that treats *molecular conformation generation* and *ground-state conformation prediction* as independent tasks. Existing approaches either generate diverse conformations but lack the ability to assess their energetic quality, or predict a single lowest-energy conformation at the cost of structural diversity. To bridge this gap, we propose the first unified framework that simultaneously produces diverse conformations and learns a faithful energy landscape, enabling reliable discrimination and selection of ground-state conformations. Building on the *Flow Matching* generative framework and *Energy-Based Models* trained with the *Energy Matching* objective, we introduce *an energy-guided flow matching scheme for non-Gaussian FM path*, substantially improving few-step ODE sampling quality from *Harmonic Prior* samples. For ground-state conformation prediction, the learned energy landscape serves as a fast and accurate surrogate for computationally expensive quantum-mechanical methods, enabling efficient lowest-energy conformation certification. Extensive experiments across multiple benchmarks demonstrate that our method consistently outperforms SOTA approaches in both few-step molecular conformation generation and ground-state conformation prediction.

References

- [1] Cristiano RW Guimarães, Alan M Mathiowetz, Marina Shalaeva, Gilles Goetz, and Spiros Liras. Use of 3d properties to characterize beyond rule-of-5 property space for passive permeation. *Journal of chemical information and modeling*, 52(4):882–890, 2012.
- [2] Christof H Schwab. Conformations and 3d pharmacophore searching. *Drug Discovery Today: Technologies*, 7(4):e245–e253, 2010.
- [3] Paul CD Hawkins. Conformation generation: the state of the art. *Journal of chemical information and modeling*, 57(8):1747–1756, 2017.
- [4] Andrew J Ballard, Stefano Martiniani, Jacob D Stevenson, Sandeep Somani, and David J Wales. Exploiting the potential energy landscape to sample free energy. *Wiley Interdisciplinary Reviews: Computational Molecular Science*, 5(3):273–289, 2015.
- [5] Marco De Vivo, Matteo Masetti, Giovanni Bottegoni, and Andrea Cavalli. Role of molecular dynamics and related methods in drug discovery. *Journal of medicinal chemistry*, 59(9):4035–4061, 2016.
- [6] Philipp Pracht, Fabian Bohle, and Stefan Grimme. Automated exploration of the low-energy chemical space with fast quantum chemical methods. *Physical Chemistry Chemical Physics*, 22(14):7169–7192, 2020.
- [7] Robert G Parr, Shridhar R Gadre, and Libero J Bartolotti. Local density functional theory of atoms and molecules. *Proceedings of the National Academy of Sciences*, 76(6):2522–2526, 1979.
- [8] P Muller et al. Glossary of terms used in physical organic chemistry. *Pure Appl. Chem*, 66(5):1077–1184, 1994.
- [9] Zhi-Hua Zhou. *Machine learning*. Springer nature, 2021.
- [10] Ethem Alpaydin. *Machine learning*. MIT press, 2021.
- [11] Christian Janiesch, Patrick Zschech, and Kai Heinrich. Machine learning and deep learning. *Electronic markets*, 31(3):685–695, 2021.
- [12] Taylan Cemgil, Sumedh Ghaisas, Krishnamurthy Dvijotham, Sven Gowal, and Pushmeet Kohli. The autoencoding variational autoencoder. *Advances in Neural Information Processing Systems*, 33:15077–15087, 2020.
- [13] Ian Goodfellow, Jean Pouget-Abadie, Mehdi Mirza, Bing Xu, David Warde-Farley, Sherjil Ozair, Aaron Courville, and Yoshua Bengio. Generative adversarial networks. *Communications of the ACM*, 63(11):139–144, 2020.
- [14] Jascha Sohl-Dickstein, Eric Weiss, Niru Maheswaranathan, and Surya Ganguli. Deep unsupervised learning using nonequilibrium thermodynamics. In *International conference on machine learning*, pages 2256–2265. pmlr, 2015.
- [15] Yang Song and Stefano Ermon. Generative modeling by estimating gradients of the data distribution. *Advances in neural information processing systems*, 32, 2019.
- [16] Jonathan Ho, Ajay Jain, and Pieter Abbeel. Denoising diffusion probabilistic models. *Advances in neural information processing systems*, 33:6840–6851, 2020.
- [17] Yaron Lipman, Ricky TQ Chen, Heli Ben-Hamu, Maximilian Nickel, and Matthew Le. Flow matching for generative modeling. In *The Eleventh International Conference on Learning Representations*, 2023.
- [18] Xingchao Liu, Chengyue Gong, and Qiang Liu. Flow straight and fast: Learning to generate and transfer data with rectified flow. *arXiv preprint arXiv:2209.03003*, 2022.
- [19] Danilo Rezende and Shakir Mohamed. Variational inference with normalizing flows. In *International conference on machine learning*, pages 1530–1538. PMLR, 2015.
- [20] Gregor NC Simm and José Miguel Hernández-Lobato. A generative model for molecular distance geometry. *arXiv preprint arXiv:1909.11459*, 2019.
- [21] Minkai Xu, Shitong Luo, Yoshua Bengio, Jian Peng, and Jian Tang. Learning neural generative dynamics for molecular conformation generation. *arXiv preprint arXiv:2102.10240*, 2021.

[22] Minkai Xu, Wujie Wang, Shitong Luo, Chence Shi, Yoshua Bengio, Rafael Gomez-Bombarelli, and Jian Tang. An end-to-end framework for molecular conformation generation via bilevel programming. In *International conference on machine learning*, pages 11537–11547. PMLR, 2021.

[23] Chence Shi, Shitong Luo, Minkai Xu, and Jian Tang. Learning gradient fields for molecular conformation generation. In *International conference on machine learning*, pages 9558–9568. PMLR, 2021.

[24] Octavian Ganea, Lagnajit Pattanaik, Connor Coley, Regina Barzilay, Klavs Jensen, William Green, and Tommi Jaakkola. Geomol: Torsional geometric generation of molecular 3d conformer ensembles. *Advances in Neural Information Processing Systems*, 34:13757–13769, 2021.

[25] Jiaqi Guan, Wesley Wei Qian, Wei-Ying Ma, Jianzhu Ma, and Jian Peng. Energy-inspired molecular conformation optimization. In *international conference on learning representations*, 2021.

[26] Minkai Xu, Lantao Yu, Yang Song, Chence Shi, Stefano Ermon, and Jian Tang. Geodiff: A geometric diffusion model for molecular conformation generation. *arXiv preprint arXiv:2203.02923*, 2022.

[27] Nathaniel Thomas, Tess Smidt, Steven Kearnes, Lusann Yang, Li Li, Kai Kohlhoff, and Patrick Riley. Tensor field networks: Rotation-and translation-equivariant neural networks for 3d point clouds. *arXiv preprint arXiv:1802.08219*, 2018.

[28] Victor Garcia Satorras, Emiel Hoogeboom, and Max Welling. E (n) equivariant graph neural networks. In *International conference on machine learning*, pages 9323–9332. PMLR, 2021.

[29] Majdi Hassan, Nikhil Shenoy, Jungyoon Lee, Hannes Stärk, Stephan Thaler, and Dominique Beaini. Et-flow: Equivariant flow-matching for molecular conformer generation. *Advances in Neural Information Processing Systems*, 37:128798–128824, 2024.

[30] Zhonglin Cao, Mario Geiger, Allan Dos Santos Costa, Danny Reidenbach, Karsten Kreis, Tomas Geffner, Franco Pellegrini, Guoqing Zhou, and Emine Kucukbenli. Efficient molecular conformer generation with so (3)-averaged flow matching and reflow. *arXiv preprint arXiv:2507.09785*, 2025.

[31] Zhao Xu, Youzhi Luo, Xuan Zhang, Xinyi Xu, Yaochen Xie, Meng Liu, Kaleb Dickerson, Cheng Deng, Maho Nakata, and Shuiwang Ji. Molecule3d: A benchmark for predicting 3d geometries from molecular graphs. *arXiv preprint arXiv:2110.01717*, 2021.

[32] Guikun Xu, Yongquan Jiang, PengChuan Lei, Yan Yang, and Jim Chen. Gtmgc: Using graph transformer to predict molecule’s ground-state conformation. In *The Twelfth International Conference on Learning Representations*, 2023.

[33] Shengjie Luo, Yixian Xu, Di He, Shuxin Zheng, Tie-Yan Liu, and Liwei Wang. Bridging geometric states via geometric diffusion bridge. *Advances in Neural Information Processing Systems*, 37:109283–109322, 2024.

[34] Fanmeng Wang, Minjie Cheng, and Hongteng Xu. Wgformer: An se (3)-transformer driven by wasserstein gradient flows for molecular ground-state conformation prediction. In *Forty-second International Conference on Machine Learning*, 2025.

[35] Taewon Kim, Hyunjin Seo, Sungsoo Ahn, and Eunho Yang. Rebind: Enhancing ground-state molecular conformation prediction via force-based graph rewiring. In *The Thirteenth International Conference on Learning Representations*, 2025.

[36] Chengxuan Ying, Tianle Cai, Shengjie Luo, Shuxin Zheng, Guolin Ke, Di He, Yanming Shen, and Tie-Yan Liu. Do transformers really perform badly for graph representation? *Advances in neural information processing systems*, 34:28877–28888, 2021.

[37] Prafulla Dhariwal and Alexander Nichol. Diffusion models beat gans on image synthesis. *Advances in neural information processing systems*, 34:8780–8794, 2021.

[38] Jonathan Ho and Tim Salimans. Classifier-free diffusion guidance. *arXiv preprint arXiv:2207.12598*, 2022.

[39] Cheng Lu, Huayu Chen, Jianfei Chen, Hang Su, Chongxuan Li, and Jun Zhu. Contrastive energy prediction for exact energy-guided diffusion sampling in offline reinforcement learning. In *International Conference on Machine Learning*, pages 22825–22855. PMLR, 2023.

[40] Hannes Stärk, Bowen Jing, Regina Barzilay, and Tommi Jaakkola. Harmonic self-conditioned flow matching for multi-ligand docking and binding site design. *arXiv preprint arXiv:2310.05764*, 2023.

[41] Yann LeCun, Sumit Chopra, Raia Hadsell, M Ranzato, Fujie Huang, et al. A tutorial on energy-based learning. *Predicting structured data*, 1(0), 2006.

[42] Michal Balcerak, Tamaz Amirashvili, Antonio Terpin, Suprosanna Shit, Lea Bogensperger, Sebastian Kaltenbach, Petros Koumoutsakos, and Bjoern Menze. Energy matching: Unifying flow matching and energy-based models for generative modeling. *arXiv preprint arXiv:2504.10612*, 2025.

[43] Simon Axelrod and Rafael Gomez-Bombarelli. Geom, energy-annotated molecular conformations for property prediction and molecular generation. *Scientific Data*, 9(1):185, 2022.

[44] Bowen Jing, Gabriele Corso, Jeffrey Chang, Regina Barzilay, and Tommi Jaakkola. Torsional diffusion for molecular conformer generation. *Advances in neural information processing systems*, 35:24240–24253, 2022.

[45] Zhiguang Fan, Yuedong Yang, Mingyuan Xu, and Hongming Chen. Ec-conf: A ultra-fast diffusion model for molecular conformation generation with equivariant consistency. *Journal of Cheminformatics*, 16(1):107, 2024.

[46] Yuyang Wang, Ahmed A Elhag, Navdeep Jaitly, Joshua M Susskind, and Miguel Angel Bautista. Swallowing the bitter pill: Simplified scalable conformer generation. *arXiv preprint arXiv:2311.17932*, 2023.

[47] Greg Landrum et al. Rdkit: A software suite for cheminformatics, computational chemistry, and predictive modeling. *Greg Landrum*, 8(31.10):5281, 2013.

[48] Weihua Hu, Bowen Liu, Joseph Gomes, Marinka Zitnik, Percy Liang, Vijay Pande, and Jure Leskovec. Strategies for pre-training graph neural networks. *arXiv preprint arXiv:1905.12265*, 2019.

[49] Shaked Brody, Uri Alon, and Eran Yahav. How attentive are graph attention networks? *arXiv preprint arXiv:2105.14491*, 2021.

[50] Ladislav Rampášek, Michael Galkin, Vijay Prakash Dwivedi, Anh Tuan Luu, Guy Wolf, and Dominique Beaini. Recipe for a general, powerful, scalable graph transformer. *Advances in Neural Information Processing Systems*, 35:14501–14515, 2022.

[51] Yaron Lipman, Marton Havasi, Peter Holderrieth, Neta Shaul, Matt Le, Brian Karrer, Ricky TQ Chen, David Lopez-Paz, Heli Ben-Hamu, and Itai Gat. Flow matching guide and code. *arXiv preprint arXiv:2412.06264*, 2024.

[52] Alexander Tong, Kilian Fatras, Nikolay Malkin, Guillaume Huguet, Yanlei Zhang, Jarrid Rector-Brooks, Guy Wolf, and Yoshua Bengio. Improving and generalizing flow-based generative models with minibatch optimal transport. *Transactions on Machine Learning Research*, pages 1–34, 2024.

[53] Ruiqi Feng, Chenglei Yu, Wenhao Deng, Peiyan Hu, and Tailin Wu. On the guidance of flow matching. *arXiv preprint arXiv:2502.02150*, 2025.

[54] Qinqing Zheng, Matt Le, Neta Shaul, Yaron Lipman, Aditya Grover, and Ricky TQ Chen. Guided flows for generative modeling and decision making. *arXiv preprint arXiv:2311.13443*, 2023.

[55] Nanye Ma, Mark Goldstein, Michael S Albergo, Nicholas M Boffi, Eric Vanden-Eijnden, and Saining Xie. Sit: Exploring flow and diffusion-based generative models with scalable interpolant transformers. In *European Conference on Computer Vision*, pages 23–40. Springer, 2024.

[56] Hyungjin Chung, Jeongsol Kim, Michael T Mccann, Marc L Klasky, and Jong Chul Ye. Diffusion posterior sampling for general noisy inverse problems. *arXiv preprint arXiv:2209.14687*, 2022.

[57] Jiaming Song, Qinsheng Zhang, Hongxu Yin, Morteza Mardani, Ming-Yu Liu, Jan Kautz, Yongxin Chen, and Arash Vahdat. Loss-guided diffusion models for plug-and-play controllable generation. In *International Conference on Machine Learning*, pages 32483–32498. PMLR, 2023.

[58] Bowen Jing, Ezra Erives, Peter Pao-Huang, Gabriele Corso, Bonnie Berger, and Tommi Jaakkola. Eigenfold: Generative protein structure prediction with diffusion models. *arXiv preprint arXiv:2304.02198*, 2023.

[59] Marco Cuturi. Sinkhorn distances: Lightspeed computation of optimal transport. *Advances in neural information processing systems*, 26, 2013.

[60] Nicolas Lanzetti, Antonio Terpin, and Florian Dörfler. Variational analysis in the wasserstein space. *arXiv preprint arXiv:2406.10676*, 2024.

[61] Nicolas Lanzetti, Saverio Bolognani, and Florian Dörfler. First-order conditions for optimization in the wasserstein space. *SIAM Journal on Mathematics of Data Science*, 7(1):274–300, 2025.

[62] Richard Jordan, David Kinderlehrer, and Felix Otto. The variational formulation of the fokker–planck equation. *SIAM journal on mathematical analysis*, 29(1):1–17, 1998.

[63] Geoffrey E Hinton. Training products of experts by minimizing contrastive divergence. *Neural computation*, 14(8):1771–1800, 2002.

[64] Philipp Thölke and Gianni De Fabritiis. Torchmd-net: equivariant transformers for neural network based molecular potentials. *arXiv preprint arXiv:2202.02541*, 2022.

[65] Anthony K Rappé, Carla J Casewit, KS Colwell, William A Goddard III, and W Mason Skiff. Uff, a full periodic table force field for molecular mechanics and molecular dynamics simulations. *Journal of the American chemical society*, 114(25):10024–10035, 1992.

[66] Thomas A Halgren. Merck molecular force field. v. extension of mmff94 using experimental data, additional computational data, and empirical rules. *Journal of Computational Chemistry*, 17(5-6):616–641, 1996.

[67] Diederik P Kingma and Max Welling. Auto-encoding variational bayes. *arXiv preprint arXiv:1312.6114*, 2013.

[68] Leo Liberti, Carlile Lavor, Nelson Maculan, and Antonio Mucherino. Euclidean distance geometry and applications. *SIAM review*, 56(1):3–69, 2014.

[69] Yang Song, Jascha Sohl-Dickstein, Diederik P Kingma, Abhishek Kumar, Stefano Ermon, and Ben Poole. Score-based generative modeling through stochastic differential equations. *arXiv preprint arXiv:2011.13456*, 2020.

[70] rdkit. Rdkit: Open-source cheminformatics, 2016. Accessed: 2025-08-07.

[71] Ashish Vaswani, Noam Shazeer, Niki Parmar, Jakob Uszkoreit, Llion Jones, Aidan N Gomez, Łukasz Kaiser, and Illia Polosukhin. Attention is all you need. *Advances in neural information processing systems*, 30, 2017.

[72] Yang Song, Prafulla Dhariwal, Mark Chen, and Ilya Sutskever. Consistency models. In *International Conference on Machine Learning*, pages 32211–32252. PMLR, 2023.

[73] Guikun Xu, Yankai Yu, Yongquan Jiang, Yan Yang, and Yatao Bian. Cofm: Molecular conformation generation via flow matching in se (3)-invariant latent space. In *ICML 2025 Generative AI and Biology (GenBio) Workshop*, 2025.

[74] Robin Rombach, Andreas Blattmann, Dominik Lorenz, Patrick Esser, and Björn Ommer. High-resolution image synthesis with latent diffusion models. In *Proceedings of the IEEE/CVF conference on computer vision and pattern recognition*, pages 10684–10695, 2022.

[75] Hongkai Zheng, Wenda Chu, Austin Wang, Nikola Kovachki, Ricardo Baptista, and Yisong Yue. Ensemble kalman diffusion guidance: A derivative-free method for inverse problems. *arXiv preprint arXiv:2409.20175*, 2024.

[76] Marcel Kollovieh, Marten Lienen, David Lüdke, Leo Schwinn, and Stephan Günnemann. Flow matching with gaussian process priors for probabilistic time series forecasting. *arXiv preprint arXiv:2410.03024*, 2024.

- [77] Shiyuan Zhang, Weitong Zhang, and Quanquan Gu. Energy-weighted flow matching for offline reinforcement learning. *arXiv preprint arXiv:2503.04975*, 2025.
- [78] Philipp Pracht, Stefan Grimme, Christoph Bannwarth, Fabian Bohle, Sebastian Ehlert, Gereon Feldmann, Johannes Gorges, Marcel Müller, Tim Neudecker, Christoph Plett, et al. Crest—a program for the exploration of low-energy molecular chemical space. *The Journal of Chemical Physics*, 160(11), 2024.
- [79] Kristof T Schütt, Huziel E Sauceda, P-J Kindermans, Alexandre Tkatchenko, and K-R Müller. Schnet—a deep learning architecture for molecules and materials. *The Journal of chemical physics*, 148(24), 2018.
- [80] Oliver T Unke and Markus Meuwly. Physnet: A neural network for predicting energies, forces, dipole moments, and partial charges. *Journal of chemical theory and computation*, 15(6):3678–3693, 2019.
- [81] Jimmy Lei Ba, Jamie Ryan Kiros, and Geoffrey E Hinton. Layer normalization. *arXiv preprint arXiv:1607.06450*, 2016.
- [82] Mostafa Dehghani, Josip Djolonga, Basil Mustafa, Piotr Padlewski, Jonathan Heek, Justin Gilmer, Andreas Peter Steiner, Mathilde Caron, Robert Geirhos, Ibrahim Alabdulmohsin, et al. Scaling vision transformers to 22 billion parameters. In *International conference on machine learning*, pages 7480–7512. PMLR, 2023.
- [83] Patrick Esser, Sumith Kulal, Andreas Blattmann, Rahim Entezari, Jonas Müller, Harry Saini, Yam Levi, Dominik Lorenz, Axel Sauer, Frederic Boesel, et al. Scaling rectified flow transformers for high-resolution image synthesis. In *Forty-first international conference on machine learning*, 2024.
- [84] Max Welling and Yee W Teh. Bayesian learning via stochastic gradient langevin dynamics. In *Proceedings of the 28th international conference on machine learning (ICML-11)*, pages 681–688, 2011.

Appendix

A Related Work & Dataset Details

A.1 Related Work

A.1.1 Molecular Conformation Generation

The task of *molecular conformation generation* entails predicting the 3D structure of molecules based on their topological graphs. In response to the efficiency limitations of traditional methods [65, 66, 7], there has been a notable shift towards data-driven approaches, particularly those leveraging deep learning techniques. Early works [20, 21, 22, 23] explored the application of VAEs [67], Normalizing Flows [19], and NCSN [15] to generate atomic distance matrices, which are subsequently converted into 3D coordinates through distance geometry methods [68]. However, these methods often produce suboptimal performance, yielding low-quality 3D structures unsuitable for practical use.

Although there are other approaches that optimize performance using various techniques [24, 25], recent advancements lead to the emergence of more powerful diffusion models [14, 16, 69]. GeoDiff [26] is the first to apply DDPM [16] for the direct generation of 3D coordinates. TorDiff [44] tries to access an RDKit-generated [70] conformation firstly and apply DDPM to its hypertorus surface. MCF [46] further improves performance by scaling a large transformer [71] instead of equivalent GNNs [27, 28, 64] for model selection, but it still suffers from sample inefficiency.

To improve sample efficiency, recent ODE-based methods, such as consistency models [72] and flow matching [17, 18, 51, 52], have been applied to generate fast and accurate conformations [45, 29, 30, 73]. ET-Flow [45] transports harmonic priors [40] to the conformation space via the Schrodinger Bridge CFM [52], achieving state-of-the-art performance. AvgFlow [30] notably contributes 1(2)-step fast sampling techniques through Reflow and Distillation [18].

A.1.2 Molecular Ground-State Conformation Prediction

Motivated by the observation that the above methods in Sec. A.1.1 generate conformations without explicit energy minimization, recent work has shifted toward deterministic prediction of molecular ground-state conformations. The work in Ref. [31] first introduced the Molecule3D benchmark, in which each molecule is paired with a high-level DFT-optimized ground-state conformation; however, the proposed task formulation is suboptimal. GTMGC [32] complements this benchmark with a more suitable task definition and strong baselines based on Graph Transformers [36], and subsequent works [33, 34] further improve performance on Molecule3D, though their experimental settings lack comparisons to generative methods, limiting comprehensiveness. ReBind [35] extends the experiments to the more comprehensive GEOM-Drugs [43] dataset by selecting, for each molecule, the conformation with the highest Boltzmann weight within its ensemble as the ground state. It then re-evaluates baselines and extends Torsional Diffusion [44] for a fairer and more comprehensive comparison. Our work is orthogonal to these approaches: we focus on enhancing generative modeling for molecular conformation generation and subsequently identify the ground state through energy-based selection. Accordingly, following ReBind [35], we evaluate ground-state conformation prediction on GEOM-Drugs and report baseline results as provided in ReBind [35].

A.1.3 Guidance in Diffusion and Flow Matching

Guided generative techniques, such as class-guided [37, 38] and energy-guided [39] modeling, have garnered significant attention within the field of generative modeling. These methods aim to generate samples that align with specific properties or classes, as opposed to merely sampling from a learned distribution [74, 57]. These techniques have been well-established in standard diffusion models [14, 15, 16, 69], which have become prominent in recent years [37, 38, 56, 74, 57, 75].

Given that flow matching [17, 18, 51] has recently emerged as a more efficient alternative to diffusion models, an increasing number of studies have begun investigating guidance mechanisms in this setting [54, 76, 77]. However, existing works largely consider flow matching with Gaussian priors, which is conceptually equivalent to diffusion models [54], and thus adopt guidance strategies that closely mirror those used in diffusion models. In contrast, a distinctive advantage of flow matching is its flexibility in transforming arbitrary prior distributions into target distributions, rather than being restricted to Gaussian priors as in diffusion models. This flexibility indicates substantial untapped potential for developing both theoretical and practical guidance approaches under non-Gaussian priors, beyond the Gaussian-based paradigm. In this direction, the recent work of Ref. [53] provides a theoretical framework that lays the foundation for such exploration.

A.2 Datasets Details

In this work, we leverage the **GEOM** [43] dataset for a comprehensive evaluation. Below, we summarize its key characteristics along four axes: molecular sources, conformation sources, conformational energy annotations, and Boltzmann weighting of conformers.

Molecular sources: GEOM consolidates drug-like compounds from AICures and multiple MoleculeNet collections, together with the QM9 small-molecule set. Canonical SMILES are produced with RDKit to merge properties from heterogeneous sources into a single molecular entry; cluster SMILES are de-salted and, when appropriate, protonated to standardize ionization states. GEOM also includes the BACE subset from MoleculeNet with experimental binding affinities, while most other biophysics sets are omitted for size reasons. Recovery of vacuum conformer–rotamer ensembles exceeds 98% for the included MoleculeNet datasets, with water-solvent ensembles generated for virtually all BACE molecules.

Conformation sources: For each molecule, an initial geometry is prepared and optimized before CREST sampling. CREST (Conformer–Rotamer Ensemble Sampling Tool) is an automated workflow for exploring low-energy conformational space via metadynamics and semiempirical quantum chemistry [78]. Drug-like molecules receive RDKit embeddings (multiple trial conformers), MMFF optimization and pruning, followed by xTB optimization; the lowest-energy xTB conformer seeds CREST. Although QM9 structures are already DFT-optimized, they are re-optimized with xTB to align with the level of theory employed by CREST. CREST then performs metadynamics under an NVT thermostat with a history-dependent RMSD-based bias; newly discovered structures along the trajectory are added as reference conformers. Multiple metadynamics runs with varied bias parameters further improve the coverage of torsional space while avoiding bond-breaking events.

Energy of conformations: The primary label for large-scale ensembles is the GFN2-xTB energy computed within CREST. A higher-accuracy route is provided for selected subsets (notably BACE), where DFT single-point energies and, in some cases, full CENSO refinements with vibrational and solvation contributions are supplied.

Boltzmann weights: Let $\lambda = 1/(k_B T)$. GEOM provides two weighting schemes. In the *CREST/xTB* protocol, each conformer i is assigned an approximate weight from its GFN2-xTB energy E_i together with an explicit degeneracy factor d_i (counting chemically equivalent rotamers),

$$w_i^{\text{xTB}} = \frac{d_i e^{-\lambda E_i}}{\sum_j d_j e^{-\lambda E_j}},$$

which serves as a proxy for free-energy probabilities and omits translational, rotational, and vibrational contributions. In the *CENSO/DFT* protocol, statistical weights are computed from conformer-specific free energies,

$$G_i = E_{\text{gas}}^{(i)} + \Delta G_{\text{solv}}^{(i)}(T) + G_{\text{trv}}^{(i)}(T), \quad w_i^{\text{DFT}} = \frac{e^{-\lambda G_i}}{\sum_j e^{-\lambda G_j}},$$

with no explicit degeneracy factor. For numerical stability, E_i or G_i can be replaced by relative values (e.g., subtracting the minimum) before evaluation.

Splitting strategies: Following recent work [29, 30] and the splitting protocol of Refs. [24, 44], evaluation is conducted on two standard GEOM subsets: **GEOM-Drugs** and **GEOM-QM9**. GEOM-Drugs contains approximately 304k drug-like molecules (mean 44 atoms), with train/validation/test splits of 243,473/30,433/1,000 molecules. GEOM-QM9 comprises approximately 120k small organic molecules (mean 11 atoms), split into 106,586/13,323/1,000 molecules for training/validation/testing. In practice, at most 30 conformers per molecule are retained by keeping the top-30 ranked by Boltzmann weight for the training and validation sets; molecules that cannot be processed by RDKit are excluded.

B Proposed Algorithms

We provide pseudocode for the main algorithms developed in our method. The overall training procedure is outlined in Alg. 1. The energy-guided sampling procedure for generating conformations is detailed in Alg. 2. Finally, the ground-state conformation certification process is described in Alg. 3.

Algorithm 1 Joint Training of EBMs with SB-CFM

- 1: **Input:** Initial $p_0(\mathcal{C}_0)$, $p_1(\mathcal{C}_1)$, $J_\phi(\mathcal{C})$ (energy model), $v_\theta(\mathcal{C}_t, t)$ (velocity field), σ (noise scale), and learning rates η_{CFM} , η_{EM} , and η_{CD} .
- 2: **Output:** Trained parameters ϕ and θ .
- 3: **Matching Phase:**
- 4: **while** not converged **do**
- 5: Sample $\mathcal{C}_0 \sim p_0(\mathcal{C}_0)$, $\mathcal{C}_1 \sim p_1(\mathcal{C}_1)$, $t \sim \mathcal{U}(0, 1)$, and noise $\epsilon \sim \mathcal{N}(0, I)$.
- 6: Compute $\mathcal{C}'_t = (1-t)\mathcal{C}_0 + t\mathcal{C}_1$; $S_t(\mathcal{C}'_t | \mathcal{C}_0, \mathcal{C}_1) = \mathcal{C}_1 - \mathcal{C}_0$.
- 7: Compute $\mathcal{C}_t = \mathcal{C}'_t + \sigma\sqrt{t(1-t)} \cdot \epsilon$; $v_t(\mathcal{C}_t | \mathcal{C}_0, \mathcal{C}_1) = \frac{1-2t}{2t(1-t)} \{\mathcal{C}_t - \mathcal{C}'_t\} + S_t$.
- 8: Compute $\mathcal{L}_{SB-CFM} = \|v_\theta(\mathcal{C}_t, t) - v_t(\mathcal{C}_t | \mathcal{C}_0, \mathcal{C}_1)\|^2$; $\mathcal{L}_{EM} = \|-\nabla_{\mathcal{C}_t} J_\phi(\mathcal{C}'_t) - S_t(\mathcal{C}'_t | \mathcal{C}_0, \mathcal{C}_1)\|^2$.
- 9: Update $\theta \leftarrow \theta - \eta_{CFM} \nabla_\theta \mathcal{L}_{SB-CFM}$; $\phi \leftarrow \phi - \eta_{EM} \nabla_\phi \mathcal{L}_{EM}$.
- 10: **end while**
- 11: **Energy Fine-tuning Phase (frozen θ):**
- 12: **while** not converged **do**
- 13: Sample $\mathcal{C}_0 \sim p_0(\mathcal{C}_0)$, $\mathcal{C}_1 \sim p_1(\mathcal{C}_1)$, and $t \sim \mathcal{U}(0, 1)$.
- 14: Compute $\mathcal{C}'_t = (1-t)\mathcal{C}_0 + t\mathcal{C}_1$; $S_t(\mathcal{C}'_t | \mathcal{C}_0, \mathcal{C}_1) = \mathcal{C}_1 - \mathcal{C}_0$.
- 15: Compute $\mathcal{L}_{EM} = \|-\nabla_{\mathcal{C}_t} J_\phi(\mathcal{C}'_t) - S_t(\mathcal{C}'_t | \mathcal{C}_0, \mathcal{C}_1)\|^2$.
- 16: Compute $\mathcal{L}_{energy} = \mathbb{E}_{\mathcal{C} \sim p_{data}(\mathcal{C})} [|J_\phi(\mathcal{C}) - E_{true}(\mathcal{C})|]$.
- 17: Update $\phi \leftarrow \phi - (\eta_{EM} \nabla_\phi \mathcal{L}_{EM} + \eta_{energy} \nabla_\phi \mathcal{L}_{energy})$.
- 18: **end while**
- 19: **Return:** Trained energy model parameters ϕ and velocity field parameters θ .

Algorithm 2 Energy-Guided Sampling for Conformation Generation

- 1: **Input:** Initial prior $p_0(\mathcal{C}_0)$, trained energy model $J_\phi(\mathcal{C})$, trained velocity field $v_\theta(\mathcal{C}_t, t)$, decay factor λ_t , number of sampling steps N , and time step $\Delta t = 1/N$.
- 2: **Output:** Generated conformations \mathcal{C}'_1 .
- 3: Set $t = 0$; initialize $\mathcal{C}_t = \mathcal{C}_0$.
- 4: **for** $i = 0$ to $N - 1$ **do**
- 5: Set $t = i \cdot \Delta t$.
- 6: Sample $\mathcal{C}_0 \sim p_0(\mathcal{C}_0)$.
- 7: Compute $\hat{\mathcal{C}}_1 = \mathcal{C}_t + (1-t)v_\theta(\mathcal{C}_t, t)$.
- 8: Compute the guided VF: $v'_t(\mathcal{C}_t) = v_\theta(\mathcal{C}_t, t) - \lambda_t \cdot \nabla_{\mathcal{C}_t} J_\phi(\hat{\mathcal{C}}_1)$.
- 9: Update conformation: $\mathcal{C}_{t+\Delta t} = \mathcal{C}_t + v'_t(\mathcal{C}_t) \cdot \Delta t$.
- 10: **end for**
- 11: **Return:** Generated conformations $\mathcal{C}'_1 = \mathcal{C}_t$.

C Model Architectures

In this section, we present the learnable neural network architecture employed in this work. To ensure consistency with the ET-Flow framework [45], we adopt the architectural design of **TorchMD-NET** [64]. It should be emphasized that the vast majority of the descriptions and technical details in this section are adapted from the ET-Flow resources [45], with minor modifications made to suit our setting. We gratefully acknowledge the authors of ET-Flow [45] for their open-source contributions.

C.1 Architecture

The architecture of the modified **TorchMD-NET** in Fig. 4(a) consists of two major components, a representation layer and an output layer. For the representation layer, a modified version of the embedding and equivariant attention-based update layers from the equivariant transformer architecture of **TorchMD-NET** [64] is used. The output layer utilizes the gated equivariant blocks from work [79]. ET-Flow [45] has made some modifications to stabilize training since it uses a larger network than the one proposed in the **TorchMD-NET** [64] paper. Additionally, since the input structures are interpolations between structures sampled from a prior and actual conformations, it is important to ensure the network is numerically stable when the interpolations contain two atoms very close to each other.

Embedding Layer: The embedding layer maps each atom’s physical and chemical properties into a learned representation space, capturing both local atomic features and geometric neighborhood information. For the i -th atom in a molecule with N atoms, we compute an invariant embedding x_i

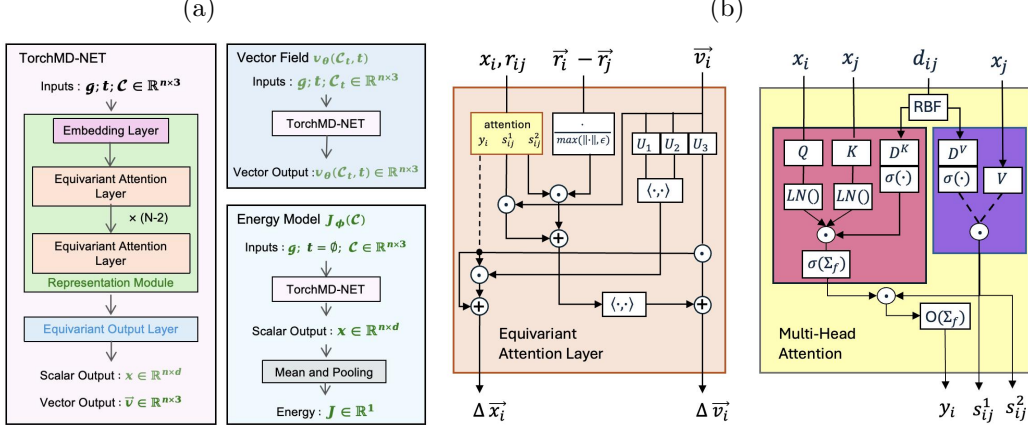


Figure 4: Model architectures in this work. (a) Following ET-Flow [45], the main learnable neural network is TorchMD-NET [64], modified to incorporate time as an additional input feature, as illustrated in the left panel. The right panel shows how TorchMD-NET is used as both a vector field model and an energy model. (b) Details of the *Equivariant Attention Layer* and *Multi-Head Attention* components in TorchMD-NET, with the illustration adapted from the ET-Flow [45] resources.

through the following process:

$$z_i = \text{embed}^{\text{int}}(z_i) \quad (31)$$

$$h_i = \text{MLP}(z_i) \quad (32)$$

where z_i is the atomic number and h_i represents atomic attributes. The MLP projects atomic attributes into a feature vector of dimension d_h .

Next, we compute a neighborhood embedding n_i that captures the local atomic environment:

$$n_i = \sum_{j=1}^N \text{embed}^{\text{nbh}}(z_j) \cdot g(d_{ij}, l_{ij}). \quad (33)$$

Here, $\text{embed}^{\text{nbh}}(z_j)$ provides a separate embedding for neighboring atomic numbers, d_{ij} is the distance between atoms i and j , and l_{ij} encodes edge features (either from a radius-based graph or molecular bonds). The interaction function $g(d_{ij}, l_{ij})$ combines distance and edge information:

$$g(d_{ij}, l_{ij}) = W^F \left[\phi(d_{ij}) e_1^{\text{RBF}}(d_{ij}), \dots, \phi(d_{ij}) e_K^{\text{RBF}}(d_{ij}), l_{ij} \right] \quad (34)$$

Algorithm 3 Ground-State Conformation Certification

- 1: **Input:** Molecular graph \mathcal{G} , trained energy model $J_\phi(\mathcal{C})$, sampler (Alg. 2), ensemble size M , mode $\in \{\text{JustFM}, \text{EnsembleCert}\}$.
- 2: **Output:** Certified ground-state conformation $\hat{\mathcal{C}}^*$.
- 3: **if** mode = **JustFM** **then**
- 4: Run Alg. 2 once with \mathcal{G} to obtain $\hat{\mathcal{C}}^*$.
- 5: **else if** mode = **EnsembleCert** **then**
- 6: Initialize $\mathcal{S} = \emptyset$.
- 7: **for** $m = 1$ **to** M **do**
- 8: Run Alg. 2 with \mathcal{G} to obtain $\mathcal{C}^{(m)}$.
- 9: $\mathcal{S} \leftarrow \mathcal{S} \cup \{\mathcal{C}^{(m)}\}$.
- 10: **end for**
- 11: $m^* \leftarrow \arg \min_{m \in \{1, \dots, M\}} J_\phi(\mathcal{C}^{(m)})$;
- 12: $\hat{\mathcal{C}}^* \leftarrow \mathcal{C}^{(m^*)}$.
- 13: **end if**
- 14: **Return:** Predicted ground-state conformation $\hat{\mathcal{C}}^*$.

Name	Description	Range
chirality	Chirality Tag	{unspecified, tetrahedral CW & CCW, other}
degree	Number of bonded neighbors	$\{x : 0 \leq x \leq 10, x \in \mathbb{Z}\}$
charge	Formal charge of atom	$\{x : -5 \leq x \leq 5, x \in \mathbb{Z}\}$
num_H	Total Number of Hydrogens	$\{x : 0 \leq x \leq 8, x \in \mathbb{Z}\}$
number_radical_e	Number of Radical Electrons	$\{x : 0 \leq x \leq 4, x \in \mathbb{Z}\}$
hybridization	Hybridization type	{sp, sp ² , sp ³ , sp ³ d, sp ³ d ² , other}
aromatic	Whether on a aromatic ring	{True, False}
in_ring	Whether in a ring	{True, False}

Table 4: Atomic features included.

where e_k^{RBF} are K exponential radial basis functions following [80], and $\phi(d_{ij})$ is a smooth cutoff function:

$$\phi(d_{ij}) = \begin{cases} \frac{1}{2} \left(\cos\left(\frac{\pi d_{ij}}{d_{\text{cutoff}}}\right) + 1 \right), & \text{if } d_{ij} \leq d_{\text{cutoff}} \\ 0, & \text{otherwise} \end{cases} \quad (35)$$

Finally, we combine all features into the atom's embedding through a linear projection:

$$x_i = W^C \left[\text{embed}^{\text{int}}(z_i), h_i, t, n_i \right], \quad (36)$$

where t represents the time-step, and $[., .]$ denotes concatenation. The resulting embedding $x_i \in \mathbb{R}^d$ serves as input to subsequent layers of the network.

Attention Mechanism: The multi-head dot-product attention operation uses atom features x_i , atom attributes h_i , time-step t and inter-atomic distances d_{ij} to compute attention weights. The input atom-level features x_i are mixed with the atom attributes h_i and the time-step t using an MLP and then normalized using a LayerNorm [81]. To compute the attention matrix, the inter-atomic distances d_{ij} are projected into two dimensional filters D^K and D^V as:

$$\begin{aligned} D^K &= \sigma \left(W^{D^K} e^{\text{RBF}}(d_{ij}) + b^{D^K} \right) \\ D^V &= \sigma \left(W^{D^V} e^{\text{RBF}}(d_{ij}) + b^{D^V} \right) \end{aligned} \quad (37)$$

The atom level features are then linearly projected along with a LayerNorm operation to derive the query Q and key K vectors. The value vector V is computed with only the linear projection of atom-level features. Applying LayerNorm on Q , K vectors (also referred to as QK-Norm) has proven to stabilize un-normalized values in the attention matrix [82, 83] when scaling networks to large number of parameters. The Q and K vectors are then used along with the distance filter D^K for a dot-product operation over the feature dimension:

$$Q = \text{LayerNorm}(W^Q x_i), \quad K = \text{LayerNorm}(W^K x_i), \quad V = W^V x_i \quad (38)$$

$$\text{dot}(Q, K, D^K) = \sum_k^F Q_k \cdot K_k \cdot D_k^K. \quad (39)$$

The attention matrix is derived by passing the above dot-product operation matrix through a non-linearity and weighting it using a cosine cutoff $\phi(d_{ij})$ (similar to the embedding layer) which ensures the attention weights are non-zero only when two atoms are within a specified cutoff:

$$A = \text{SiLU}(\text{dot}(Q, K, D^K)) \cdot \phi(d_{ij}). \quad (40)$$

Using the value vector V and the distance filter D_V , we derive 3 equally sized filters by splitting along the feature dimension,

$$s_{ij}^1, s_{ij}^2, s_{ij}^3 = \text{split}(V_j \cdot D_V^V). \quad (41)$$

A linear projection is then applied to combine the attention matrix and the vectors s_{ij}^3 to derive an atom level feature $y_i = W^O \left(\sum_j^N A_{ij} \cdot s_{ij}^3 \right)$. The output of the attention operation are y_i (an atom level feature) and two scalar filters s_{ij}^1 and s_{ij}^2 (edge-level features).

Update Layer: The update layer computes interactions between atoms in the attention block and uses the outputs to update the scalar feature x_i and the vector feature \vec{v}_i . First, the scalar feature output y_i from the attention mechanism is split into three features (q_i^1, q_i^2, q_i^3) , out of which q_i^1 and q_i^2 are used for the scalar feature update as,

$$\Delta x_i = q_i^1 + q_i^2 \cdot \langle U_1 \vec{v}_i \cdot U_2 \vec{v}_i \rangle, \quad (42)$$

where $\langle U_1 \vec{v}_i \cdot U_2 \vec{v}_i \rangle$ is the inner product between linear projections of vector features \vec{v}_i with matrices U_1, U_2 .

The edge vector update consists of two components. First, we compute a vector \vec{w}_i , which for each atom is computed as a weighted sum of vector features and a clamped-norm of the edge vectors over all neighbors:

$$\vec{w}_i = \sum_j^N s_{ij}^1 \cdot \vec{v}_j + s_{ij}^2 \cdot \frac{\vec{r}_i - \vec{r}_j}{\max(\|\vec{r}_i - \vec{r}_j\|, \epsilon)}, \quad (43)$$

$$\Delta \vec{v}_i = \vec{w}_i + q_i^3 \cdot U_3 \vec{v}_i \quad (44)$$

where U_1 and U_3 are projection matrices over the feature dimension of the vector feature \vec{v}_i . In this layer, we clamp the minimum value of the norm (to $\epsilon = 0.01$) to prevent numerically large values in cases where positions of two atoms are sampled too close from the prior.

$SO(3)$ Update Layer: We also design an $SO(3)$ equivariant architecture by adding an additional cross product term in Eq. 43 as follows,

$$\vec{w}_i = \sum_j^N s_{ij}^1 \cdot \vec{v}_j + s_{ij}^2 \cdot \frac{\vec{r}_i - \vec{r}_j}{\max(\|\vec{r}_i - \vec{r}_j\|, \epsilon)} + s_{ij}^4 \cdot \left(\vec{v}_j \times \frac{\vec{r}_i - \vec{r}_j}{\max(\|\vec{r}_i - \vec{r}_j\|, \epsilon)} \right), \quad (45)$$

where s_{ij}^4 is derived by modifying the split operation Eq. 41 in the attention layer where the value vector V and distance filter D_V is projected into 4 equally sized filters instead of 3.

Output Layer: The output layer consists of Gated Equivariant Blocks from [79]. Given atom scalar features x_i and vector features \vec{v}_i , the updates in each block is defined as,

$$x_{i,\text{updated}}, \vec{w}_i = \text{split}(\text{MLP}([x_i, U_1 \vec{v}_i])) \quad (46)$$

$$\vec{v}_{i,\text{updated}} = (U_2 \vec{v}_i) \cdot \vec{w}_i \quad (47)$$

Here, U_1 and U_2 are linear projection matrices that act along feature dimension. Our modification is to use LayerNorm in the MLP to improve training stability.

C.2 Input Featurization

Following ET-Flow [45], atomic (node) features are computed using RDKit [47] descriptors, as detailed in Tab. 4. To construct the edge features and edge index, we employ a combination of global radius-based edges and local molecular-graph edges, similar to the approach in Ref. [44].

D More Details and Experiments

D.1 Implementation Details

D.1.1 Reflow Technique

Following AvgFlow [30], which adopts a Reflow technique [18] to improve the conformation sampling quality with a single ODE step, we also implement a Reflow procedure in our experiments. Specifically, after the main training phase is completed, we first randomly sample a fixed number of prior samples \mathcal{C}'_0 from the harmonic prior distribution for each molecule in the training and validation sets. We then apply a fixed number of ODE steps to generate the corresponding conformation samples \mathcal{C}'_1 . Finally, the coupled pairs $(\mathcal{C}'_0, \mathcal{C}'_1)$ are used to further fine-tune the trained model with the reflow loss:

$$\mathcal{C}'_t = (1-t)\mathcal{C}'_0 + t\mathcal{C}'_1 + \sigma \sqrt{t(1-t)} \cdot \epsilon, \quad \epsilon \sim \mathcal{N}(0, I). \quad (48)$$

$$v_t(\mathcal{C}'_t | \mathcal{C}'_0, \mathcal{C}'_1) = \frac{1-2t}{2t(1-t)} (\sigma \sqrt{t(1-t)} \cdot \epsilon) + (\mathcal{C}'_1 - \mathcal{C}'_0). \quad (49)$$

$$\mathcal{L}_{\text{Reflow}} = \mathbb{E}_{\mathcal{C}'_t \sim p_t(\mathcal{C}'_t | \mathcal{C}'_0, \mathcal{C}'_1), t \sim \mathcal{U}(0, 1)} \left[\|v_\theta(\mathcal{C}'_t, t) - v_t(\mathcal{C}'_t | \mathcal{C}'_0, \mathcal{C}'_1)\|^2 \right]. \quad (50)$$

	1 ODE step	2 ODE steps	5 ODE steps	50 ODE steps
GEOM-Drugs	$0.5(1-t)^2$	$0.3(1-t)^2$	$0.2(1-t)^2$	$0.1(1-t)^2$
GEOM-QM9	$0.4(1-t)^2$	$0.3(1-t)^2$	$0.2(1-t)^2$	$0.1(1-t)^2$

Table 5: Guidance schedule λ_t under different numbers of ODE sampling steps.

It is worth noting that we apply the reflow technique only to the vector field model v_θ , i.e., the unguided path. After reflow fine-tuning, we use the same guided sampling algorithm described in Alg. 2 for inference as before, but employing the newly reflowed vector field model.

D.1.2 Traing Details

For GEOM-Drugs, during the first *matching phase*, EnFlow is trained for 500 epochs with a batch size of 24, capped at 5,000 batches per epoch, on 6 NVIDIA A100 GPUs. During the second *energy fine-tuning phase*, EnFlow is again trained for 500 epochs with a batch size of 48, limited to 5,000 batches per epoch, on 4 NVIDIA A100 GPUs. We use the AdamW optimizer with a cosine-annealed learning rate schedule ranging from 1×10^{-8} to 5×10^{-4} for both phases. For GEOM-QM9, in the first *matching phase*, EnFlow is trained for 1,000 epochs with a batch size of 48, capped at 1,000 batches per epoch, on 8 NVIDIA A100 GPUs. In the second *energy fine-tuning phase*, EnFlow is trained for 1,000 epochs with a batch size of 64, again limited to 1,000 batches per epoch, on 4 NVIDIA A100 GPUs. For GEOM-QM9, we also use the AdamW optimizer with a cosine-annealed learning rate schedule ranging from 1×10^{-8} to 7×10^{-4} . For both datasets, the best checkpoint is selected based on the lowest validation loss.

D.1.3 Reproduction Issues of ET-Flow

As EnFlow builds upon ET-Flow [45], we have made every effort to reproduce the reported results of ET-Flow on GEOM-Drugs and GEOM-QM9. However, as shown in Tab. 1 and Tab. 2 of the main paper, we observe a noticeable performance gap between our reproduced results and those originally reported, especially on GEOM-Drugs. Several relevant issues have been raised in ET-Flow’s official GitHub repository (<https://github.com/shenoynikhil/ETFlow.git>), and the authors have acknowledged these concerns. We thank the authors for their helpful communication and support during our reproduction attempts, and we leave a more detailed investigation of this gap as an open problem for future work.

D.1.4 Choice of the Guidance Schedule

As formulated in Eq. 29, we perform energy-guided sampling using the guided vector field $v_t'(\mathcal{C}_t)$. The guidance strength λ_t is chosen as a time-dependent decay factor that vanishes as $t \rightarrow 1$. In our experiments, we adopt a simple quadratic schedule, as summarized in Tab. 5. There are more discussion on these choice in Sec. D.2.1.

D.2 More Experimental Results

D.2.1 Observations on the Guidance Schedule

In Sec. D.1.4, we outline the guidance schedule employed in our experiments. A natural question arises as to why relatively small guidance strengths are selected for the 5-step and 50-step ODE samplers. To justify this design choice, we perform an ablation study over a range of guidance strengths λ_t under both settings. The quantitative results and metric curves are summarized in Fig. 5.

The ablation results reveal a clear trade-off governed by the magnitude of the guidance. As the guidance strength increases, the Recall-oriented metrics (COV-R and AMR-R) exhibit a consistent degradation, whereas the Precision-oriented metrics (COV-P and AMR-P) improve substantially, with the improvements being most pronounced at small RMSD thresholds δ . At the same time, the mean predicted energy J_ϕ decreases markedly, indicating that stronger guidance biases the sampling process toward lower-energy regions of the conformational landscape. Consequently, higher-energy conformations become underrepresented, while the generated structures align more closely with low-energy reference conformations.

This behavior suggests that increasing the guidance strength makes the sampler more conservative: it preferentially generates energetically favorable structures—thereby enhancing Precision—but at the expense of structural diversity, which leads to reduced Recall across RMSD thresholds. Because

our primary objective is to attain high-quality conformations with very few ODE steps, we adopt moderate guidance strengths for the 5-step and 50-step settings. This choice yields a more balanced trade-off between Recall and Precision, enabling fair comparison with existing baselines while still leveraging the benefits of energy-guided sampling.

D.2.2 Why Energy-Matching Training Is Necessary for the Energy Model

Since our primary objective is to employ the energy-guided vector field $v'_t(\mathcal{C}_t, t)$ to yield the guided probability path $p'_t(\mathcal{C}_t)$, rather than relying on the original unguided vector field $v_\theta(\mathcal{C}_t, t)$ that produces the unguided path $p_t(\mathcal{C}_t)$, it is essential that the learned energy model provides accurate and well-calibrated gradients. Both vector fields transport the same source distribution (the Harmonic prior $p_0(\mathcal{C}_0)$) but toward different targets, $p_1(\mathcal{C}_1) e^{-J_\phi(\mathcal{C}_1)}$ for the guided case and $p_1(\mathcal{C}_1)$ for the unguided case. While the energy regression loss $\mathcal{L}_{\text{energy}}$ encourages the model $J_\phi(\mathcal{C})$ to approximate absolute energies, it does not guarantee that energy *differences* are preserved, which are crucial for inducing correct gradient directions. In contrast, the *Energy Matching* loss \mathcal{L}_{em} explicitly aligns predicted and true energy differences, yielding faithful gradients from Harmonic-prior samples toward lower-energy conformations.

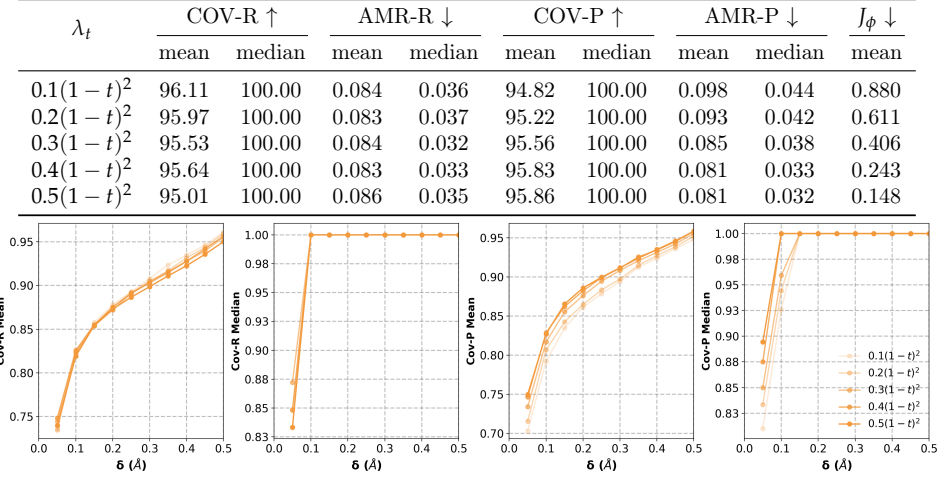
The necessity of *Energy Matching* [42] is confirmed empirically in Fig. 5. For both the 2-step and 5-step ODE samplers, using only the unguided vector field $v(\mathcal{C}_t, t)$ leads to high Recall (COV-R and AMR-R) but noticeably weaker Precision (COV-P and AMR-P), indicating poor energetic consistency. Adding guidance via $v'_t(\mathcal{C}_t, t)$ with only $\mathcal{L}_{\text{energy}}$ yields only modest gains, reflecting unreliable gradient directions. In contrast, training the energy model with both $\mathcal{L}_{\text{energy}}$ and \mathcal{L}_{em} consistently improves all metrics: Recall- and Precision-oriented scores increase simultaneously, and the curves across RMSD thresholds show clear and stable gains. These results demonstrate that *Energy Matching* is essential for obtaining reliable energy gradients and for enabling effective energy-guided ODE sampling.

D.2.3 Ablation Studies on the Choice of the Vector Field for Sampling

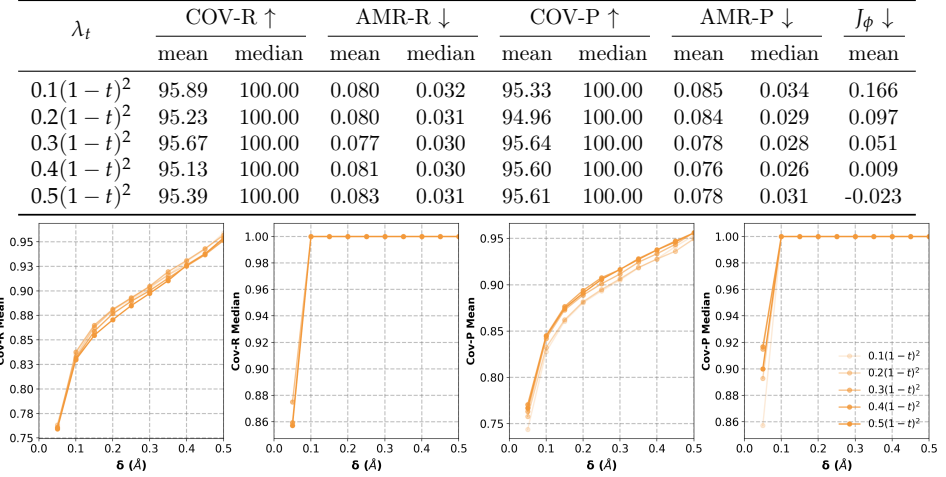
To further validate the robustness of our proposed guided vector field v' , we conduct ablation studies comparing three vector fields for ODE sampling: (1) the unguided vector field $v_\theta(\mathcal{C}_t, t)$, corresponding to the pure flow-matching framework in ET-Flow [29]; (2) the pure energy-gradient field $-\nabla_{\mathcal{C}_t} J_\phi(\mathcal{C}_t)$, representing a straight-path flow-matching formulation as in Ref. [18] with a *time-independent* vector field, or equivalently, deterministic Langevin dynamics [84] without noise (i.e., Gradient Descent); and (3) our proposed energy-guided vector field $v_\theta(\mathcal{C}_t, t) - \lambda_t \nabla_{\hat{\mathcal{C}}_1} J_\phi(\hat{\mathcal{C}}_1)$. The quantitative results and metric trajectories are presented in Fig. 7.

The ablation results in Fig. 7 consistently demonstrate the superiority of our proposed energy-guided vector field across different datasets and ODE sampling budgets. Compared with the unguided flow-matching vector field $v_\theta(\mathcal{C}_t, t)$, our method achieves substantially lower AMR-R and AMR-P values, indicating that the generated conformers more closely match the reference structures. At the same time, the coverage metrics (COV-R and COV-P) remain comparable or slightly improved, showing that the introduction of energy guidance does not compromise diversity. In contrast, the pure energy-gradient field $-\nabla_{\mathcal{C}_t} J_\phi(\mathcal{C}_t)$ exhibits pronounced degradation in both coverage and accuracy, confirming that relying solely on the EBM leads to oversmoothing and poor generative behavior. Notably, our method consistently yields much lower mean predicted energies J_ϕ , reflecting its ability to steer samples toward physically meaningful low-energy regions. These trends persist across 2-step and 5-step sampling on GEOM-QM9 and 5-step sampling on GEOM-Drugs, demonstrating that the proposed guided vector field enhances both the stability and fidelity of ODE-based sampling, particularly under few-step regimes.

(a) 5 ODE steps sampling on GEOM-QM9



(b) 50 ODE steps sampling on GEOM-QM9



(c) 5 ODE steps sampling on GEOM-Drugs

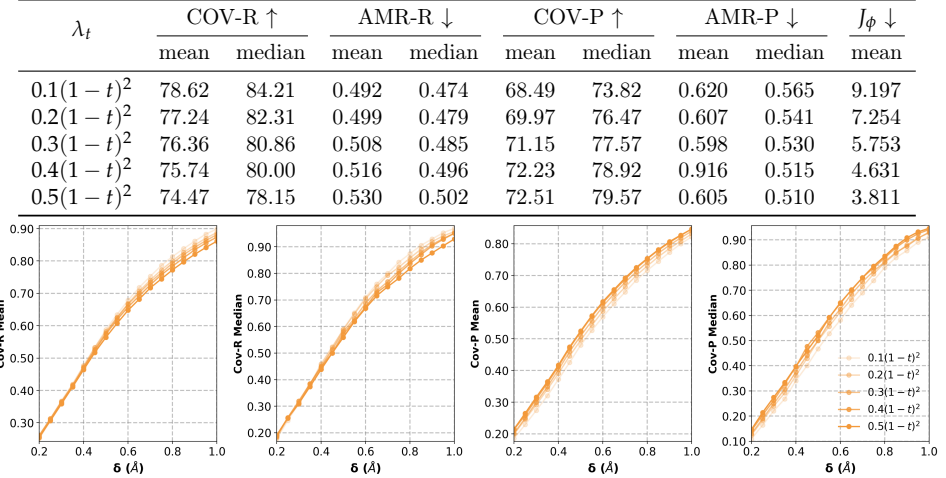
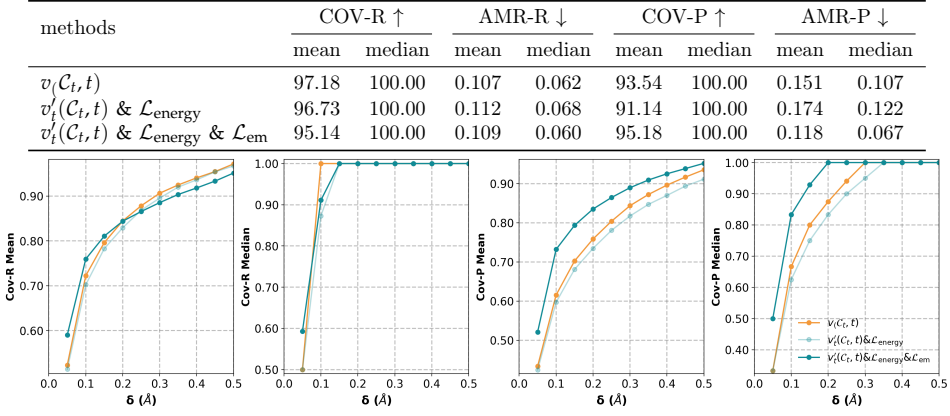


Figure 5: Ablation study of guidance strengths λ_t for 5-step (a) and 50-step (b) ODE sampling on GEOM-QM9, and for 5-step (c) ODE sampling on GEOM-Drugs. The table reports Recall and Precision metrics at a fixed RMSD threshold of $\delta = 0.5 \text{ \AA}$ for GEOM-QM9 and $\delta = 0.75 \text{ \AA}$ for GEOM-Drugs, together with the mean predicted energy J_ϕ . The plots depict how these metrics vary as a function of the RMSD threshold δ .

(a) 2 ODE steps sampling on GEOM-QM9



(b) 5 ODE steps sampling on GEOM-QM9

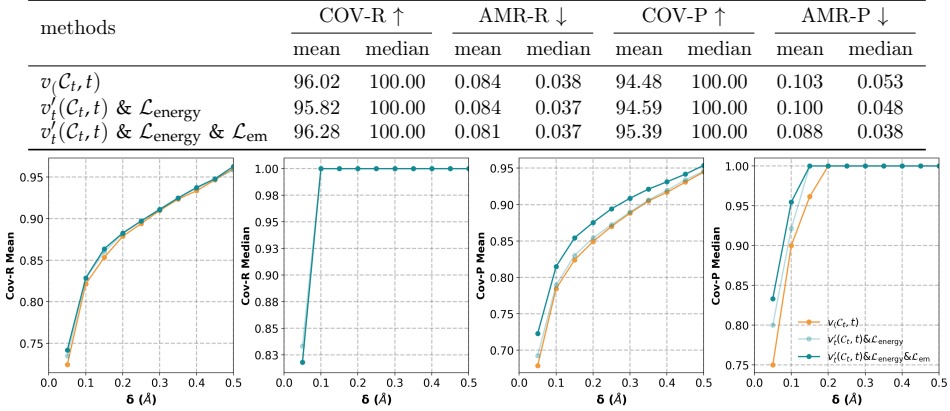
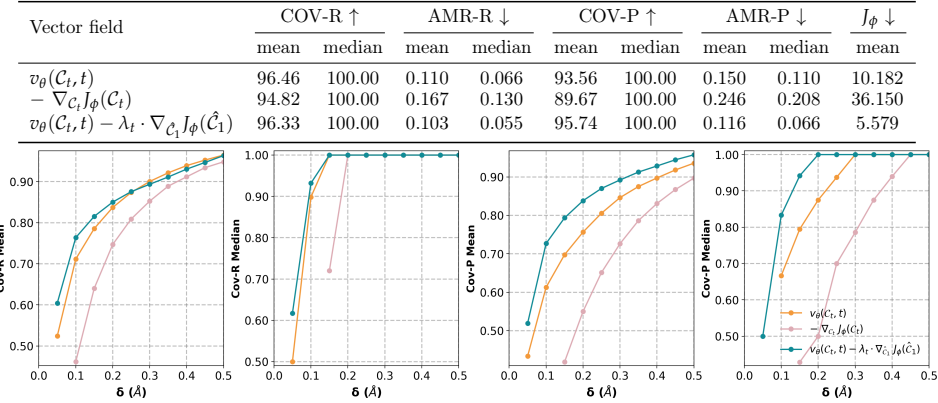
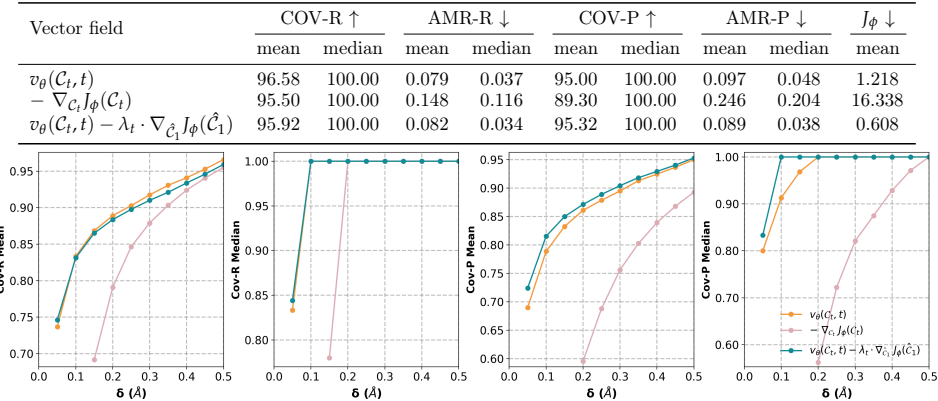


Figure 6: Ablation study on the necessity of *Energy Matching* training. For 2-step (a) and 5-step (b) ODE sampling on GEOM-QM9, the table reports Recall and Precision metrics at a fixed RMSD threshold $\delta = 0.5 \text{ \AA}$, and the plots depict how these metrics vary as a function of the RMSD threshold δ .

(a) 2 ODE steps sampling on GEOM-QM9



(b) 5 ODE steps sampling on GEOM-QM9



(c) 5 ODE steps sampling on GEOM-Drugs

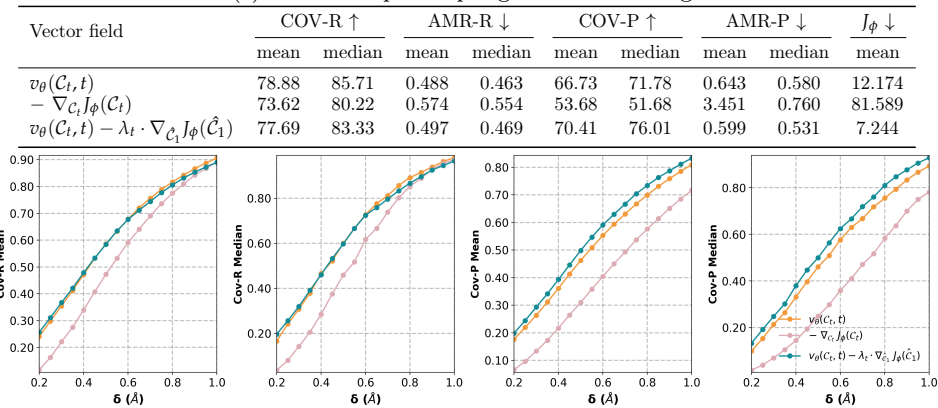


Figure 7: Ablation study of different types of vector fields for 2-step (a) and 5-step (b) ODE sampling on GEOM-QM9, and for 5-step (c) ODE sampling on GEOM-Drugs. The table reports Recall and Precision metrics at a fixed RMSD threshold of $\delta = 0.5 \text{ \AA}$ for GEOM-QM9 and $\delta = 0.75 \text{ \AA}$ for GEOM-Drugs, together with the mean predicted energy J_ϕ . The plots depict how these metrics vary as a function of the RMSD threshold δ .

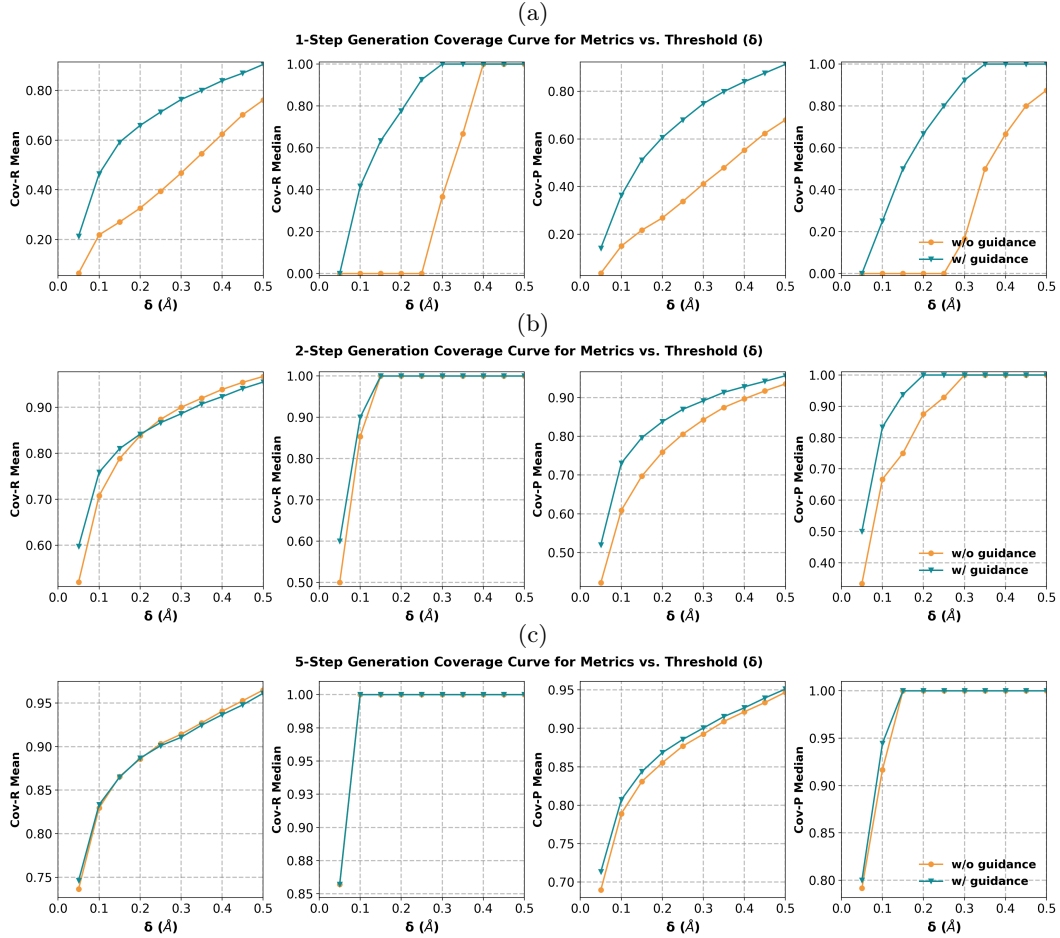


Figure 8: Ablation study of coverage (%) vs. threshold δ on the GEOM-QM9 dataset for ODE sampling with 1 (a), 2 (b) and 5 (c) steps, comparing the unguided baseline (ET-Flow; **w/o guidance**) with the guided model (**EnFlow**; **w/ guidance**).

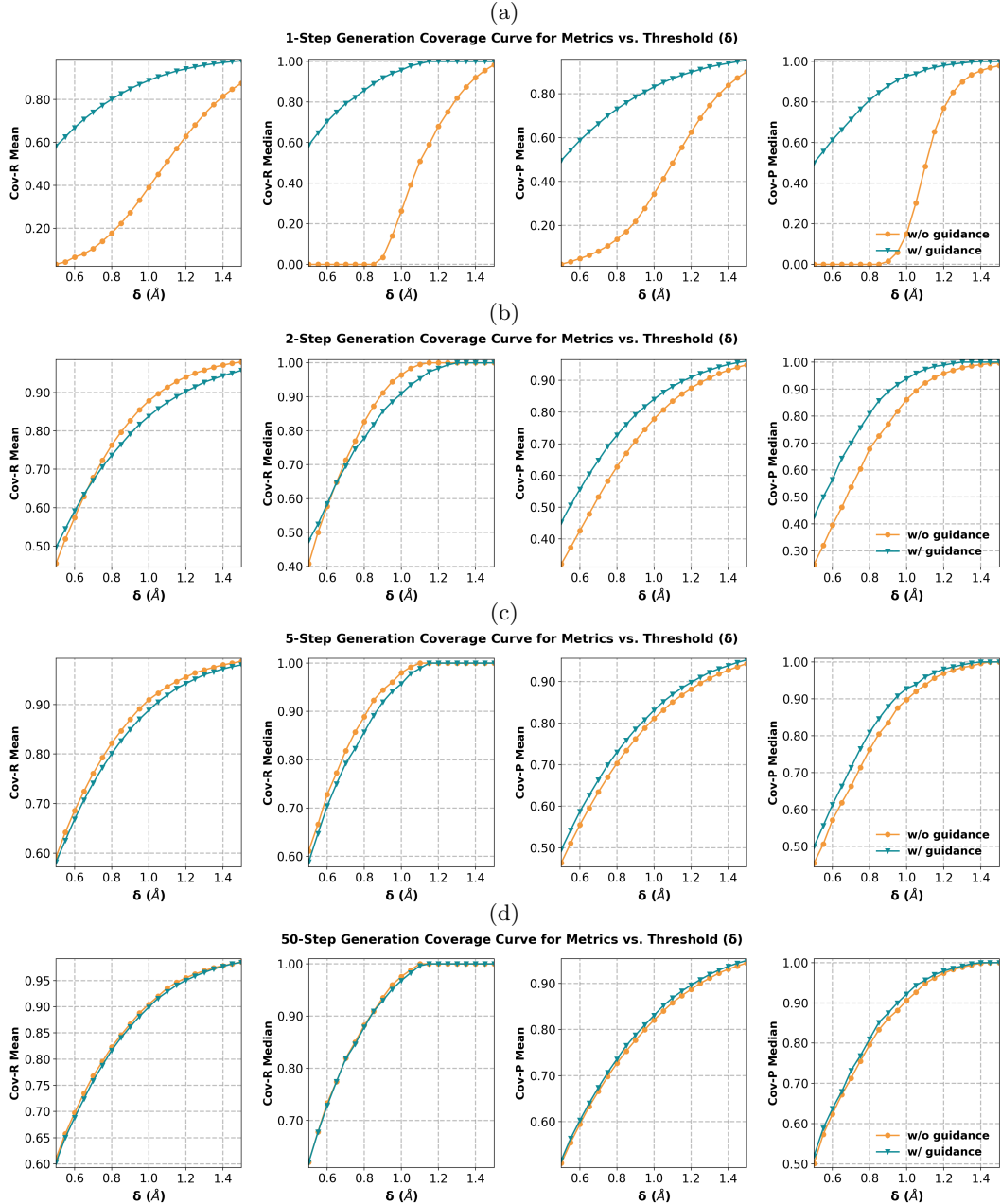


Figure 9: Ablation study of coverage (%) vs. threshold δ on the GEOM-Drugs dataset for ODE sampling with 1 (a), 2 (b), 5 (c), and 50 (d) steps, comparing the unguided baseline (ET-Flow; **w/o guidance**) with the guided model (EnFlow; **w/ guidance**).

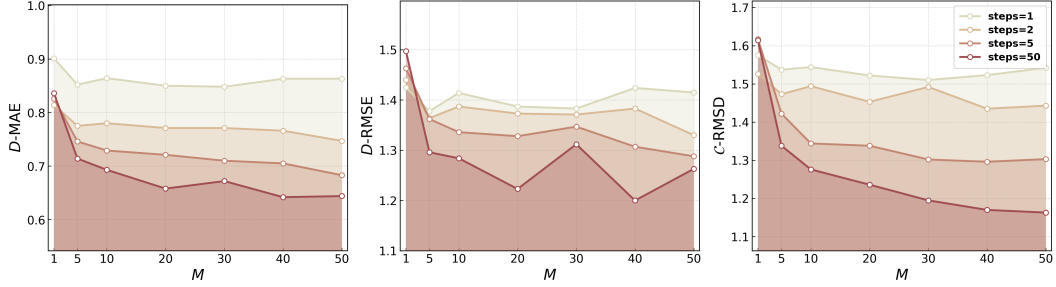


Figure 10: Ablation of **EnsembleCert** mode for ground-state conformation prediction on the GEOM-Drugs dataset. Effect of ensemble size $M = 1, 5, 10, 20, 50$ under 1, 2, 5, and 50 ODE sampling steps. From left to right: $D\text{-MAE}$ (Å), $D\text{-RMSE}$ (Å), $C\text{-RMSD}$ (Å).

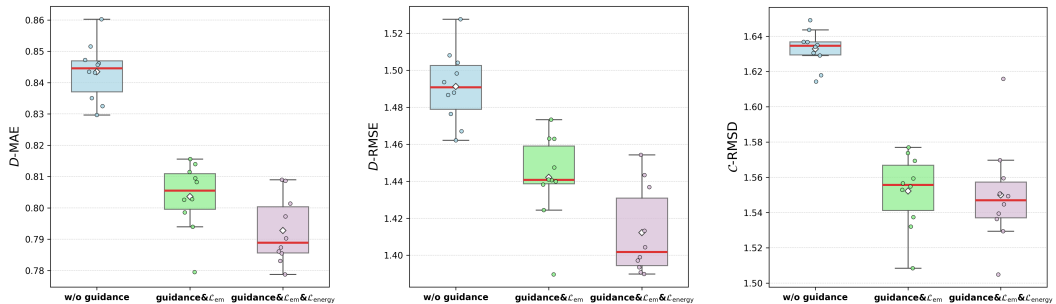


Figure 11: With JustFM mode and 5-step ODE sampling, boxplots of ground-state conformation prediction performance under three settings: (1) unguided baseline (ET-Flow; **w/o guidance**); (2) guided model with energy matching only (**guidance & \mathcal{L}_{em}**); and (3) fully guided model with energy matching and energy fine-tuning (**EnFlow**; **guidance & \mathcal{L}_{em} & $\mathcal{L}_{\text{energy}}$**).

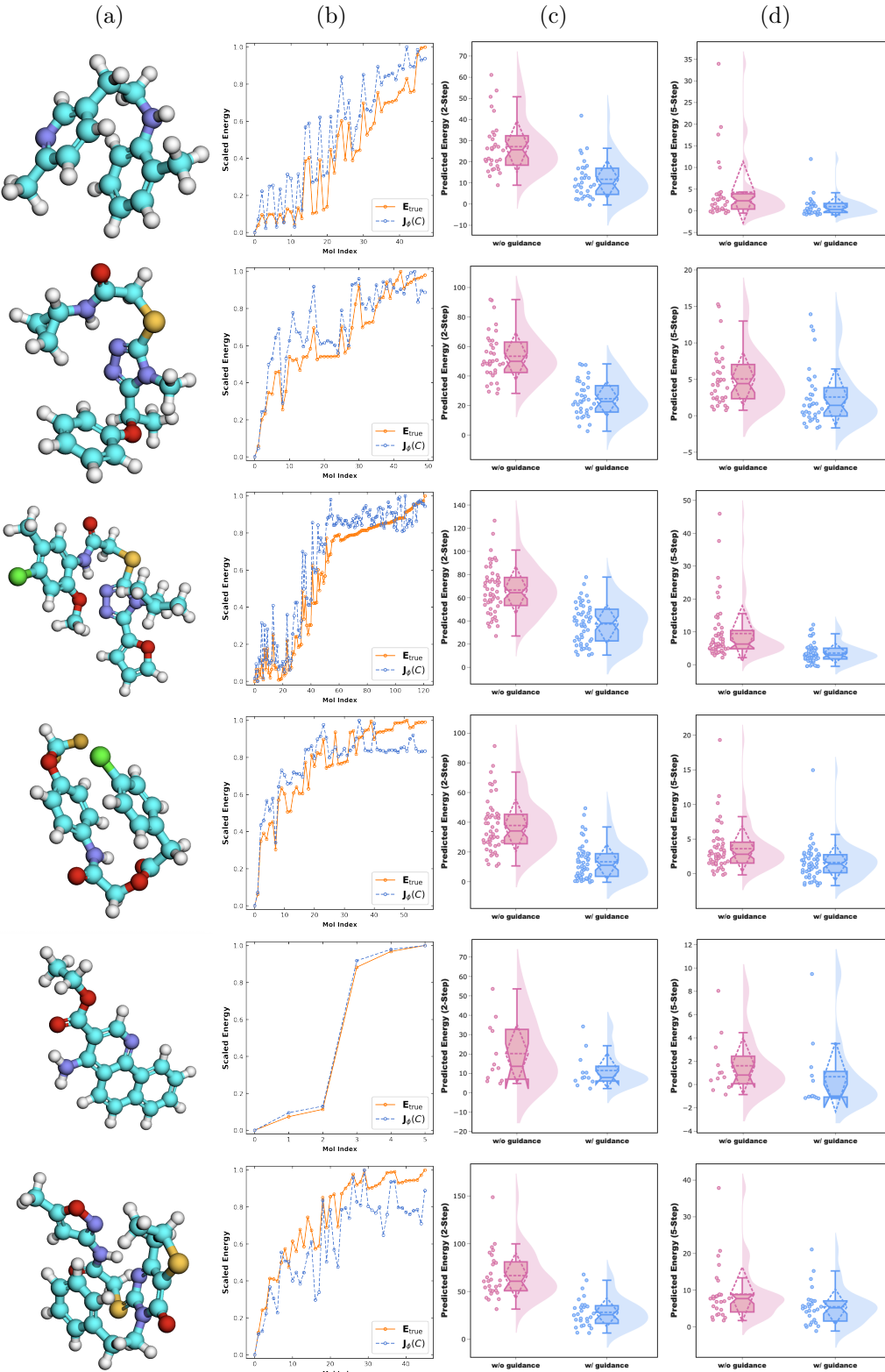


Figure 12: (a) Six representative molecules from the GEOM-Drugs dataset. (b) Their energy landscapes (Molecules are ranked by default using the true Boltzmann weights from the dataset): E_{true} denotes the ground-truth energy values from the dataset, computed by high-level quantum-chemical methods, and $J_\phi(C)$ denotes the learned energy landscape given by our EBM J_ϕ . Both are normalized to the range $[0, 1]$ to make their variation comparable. (c)–(d) Predicted energies from J_ϕ for generated conformations along two sampling trajectories with 2 steps (c) and 5 steps (d) for each molecule. The unguided baseline (ET-Flow; **w/o guidance**) is shown in red, and the guided model (**EnFlow; w/ guidance**) is shown in blue.